Identification of SPP1-positive macrophages by single-cell spatial analysis in human lung tissues with mycobacterial infection

Harutaka Katano[1], Akira Hebisawa[2], Yuko Sato[1], Yoshihiko Hoshino[3]

[1]Department of Pathology, National Institute of Infectious Diseases, Tokyo, Japan.
[2]Clinical Research Center, National Hospital Organization Tokyo National Hospital, Tokyo, Japan.
[3]Department of Mycobacteriology, Leprosy Research Center, National Institute of Infectious Diseases, Tokyo, Japan.

Address for correspondence: Harutaka Katano, Department of Pathology, National Institute of Infectious Diseases, 1-23-1 Toyama, Shinjuku, Tokyo 162-8640, Japan. e-mail: katano@niid.go.jp and Yoshihiko Hoshino, Department of Mycobacteriology, Leprosy Research Center, National Institute of Infectious Diseases, 4-2-1 Aoba, Higashi-Murayama, Tokyo, 189-0002, Japan e-mail: yhoshino@niid.go.jp

Abstract

Tuberculosis and non-tuberculous mycobacterial (NTM) diseases are infections caused by *Mycobacterium tuberculosis* and non-tuberculous mycobacteria such as *Mycobacterium avium* complex, leading to the formation of granulomatous lesions with caseous necrosis in the lungs. Although granulomatous tissues are infiltrated by numerous inflammatory cells, including macrophages, lymphocytes, and neutrophils, the mechanisms underlying granuloma formation by mycobacteria remain unclear. In this study, we performed single-cell spatial analysis on lung tissue samples from patients with tuberculosis and NTM diseases to investigate the infiltrating cell populations. We analyzed seven lung lesions and identified individual cell types infiltrating the granulomatous tissue. Based on gene expression profiles, at least four macrophage subtypes were identified. Notably, SPP1-positive macrophages predominantly infiltrated the granulomatous tissue. Langhans giant cells expressed SPP1, and many SPP1-positive macrophages without giant cell morphology were also present around the granuloma. RNA-seq analysis revealed elevated SPP1 expression in mycobacterium-infected tissues. The SPP1-CD44 signaling pathway was active in SPP1-positive macrophages and their neighboring cells in mycobacterium-infected tissues. SPP1-positive macrophages were also observed around granulomas in other granulomatous diseases, such as granulomatosis with polyangiitis and sarcoidosis. These findings suggest that SPP1-positive macrophages may play a key role in granuloma formation in granulomatous diseases, including mycobacterial infections.

INTRODUCTION

Tuberculosis and non-tuberculous mycobacterial (NTM) diseases, caused by *Mycobacterium tuberculosis* and various non-tuberculous mycobacteria—particularly the *Mycobacterium avium intracellulare* complex (MAC)—represent significant public health challenges[1]. These infections predominantly affect the lungs, leading to the formation of granulomatous lesions, which are characterized by caseous necrosis[2]. Despite extensive research efforts, the mechanisms underlying granuloma formation in mycobacterial infections remain largely enigmatic and poorly understood[3-5].

Granulomas are highly organized structures that form in response to persistent pathogens. These cellular conglomerates, composed of immune cells such as macrophages, lymphocytes, and neutrophils, aim to contain and neutralize the pathogen, serving as a barrier to prevent its spread[2,4,6]. Immunohistochemical and special staining techniques have detected mycobacterial antigens within the caseous necrotic tissue of granulomas, supporting the hypothesis that granulomas play a crucial role in controlling the dissemination of mycobacteria[3]. However, the precise formation and dynamic regulation of these structures, particularly in the context of mycobacterial infections, remain incompletely understood.

Various immune cells, including macrophages, B cells, T cells, NK cells, dendritic cells, and neutrophils, participate in granuloma formation.[2,7]. Among these, macrophages are pivotal, exhibiting remarkable plasticity that allows them to adapt to a wide range of environmental stimuli. During mycobacterial infections, macrophages can assume diverse functional states, contributing both to pathogen clearance and, paradoxically, to pathogen survival[3,4,8,9]. Macrophages, along with dendritic cells and alveolar epithelial cells, phagocytize mycobacteria during the initial stages of infection. The immune response to mycobacteria triggers several signaling pathways, including IFN-γ and TLR2 signaling, which promote the production of pro-inflammatory cytokines such as IL-12, IL-23, and TNF-α. These signals, particularly through TLR2, ultimately contribute to the formation of granulomas.[8,10-13].

To gain insight into the cellular responses to mycobacterial infections in the lung, it is critical to identify the specific cell types infiltrating granulomas and to characterize their dynamic interactions. To this end, we employed the cutting-edge Nanostring CosMx™ platform to perform single-cell spatial analysis on lung tissue samples from patients with MTB or NTM diseases.[14]. This advanced technology enabled us to map and identify individual cell types surrounding the granulomatous tissue. In addition, single-cell spatial

77 analysis allowed for detailed gene expression profiling within individual cells, providing
78 insights into the localization of cells and the identification of key signaling pathways
79 involved in cell-cell communication within the tissue microenvironment. This innovative
80 approach holds promise for unraveling the complex interplay of immune cells during
81 MTB and NTM infections.
82 In our study, we applied single-cell spatial analysis to explore the cellular landscape of
83 lung tissue samples from patients with MTB or NTM infections, with a particular
84 emphasis on macrophages and their critical role in granuloma formation.
85
86
87 **RESULTS**
88 **Cell typing in lung tissues with mycobacterial infection**
89 Seven lung tissue samples from patients with MTB (n = 3) and NTM (n = 4) infections
90 were analyzed using the Nanostring CosMx™ platform (Supplementary Table 1). Each
91 slide contained granulomas with inflammatory cell infiltrates, including foreign body
92 macrophages (Langhans giant cells, Supplementary Figures 1a and 1b).
93 Immunohistochemistry and Ziehl-Neelsen staining demonstrated that mycobacteria
94 bacilli were predominantly detected in the center of the granulomas, but were absent in
95 the surrounding inflammatory cell infiltrates in both NTM and MTB samples
96 (Supplementary Figure 2). CosMx™ analysis identified a total of 300,841 cells across the
97 seven slides (Supplementary Table 2). Cluster analysis revealed 26 distinct clusters based
98 on gene expression profiles (Figure 1). Differentially expressed gene (DEG) analysis
99 identified 520 cluster-specific marker genes with adjusted p-values. These DEGs (gene
100 lists available in Supplementary Data: marker_heatmap_nb_clus_4.csv) were used to
101 annotate subpopulations. The cell types within each cluster were determined by SingleR.
102 Neutrophil and B-cell lineages were manually annotated based on gene expression data
103 from the Human Gene Atlas (Gene Set Enrichment Analysis, GSEA, https://www.gsea-
104 msigdb.org/gsea/index.jsp). The proportions of cell types varied across samples and fields
105 of view (FoVs) (Figure 1E and Supplementary Figures 3-5).
106 Through in silico analysis based on gene expression, at least four subtypes (a-d) of
107 macrophages were identified. Macrophage subtypes were categorized based on the
108 expression of specific markers such as CD14, CD163, CD68, and LYZ. Macrophage
109 subtypes *a*, *b*, and *c* were classified conventionally as M1, M2, and M2 macrophages,
110 respectively (Figures 2A and 3B). Macrophage subtype *d*, which expressed CCR7 and
111 did not express CD163 (suggesting an M1 phenotype), predominantly expressed SPP1
112 and MARCO (Figures 2A-D). Consequently, this subtype was designated as SPP1-

113 positive macrophages. SPP1-positive macrophages were present in all NTM and MTB
114 slides, although their abundance varied among the samples (Figure 1E, Supplementary
115 Table 3).

116 **SPP1 macrophages infiltrate around MTB and NTM granuloma**

117 CosMx™ spatial imaging revealed that SPP1-positive macrophages predominantly
118 infiltrated the periphery of NTM-positive granulomatous tissue (Figure 3, Supplementary
119 Figures 6a and 6b). In MTB-infected tissues, SPP1-positive macrophages were also
120 observed in the interstitial regions and alveolar spaces (Figure 4, Supplementary Figure
121 6c). Both CosMx™ spatial images and immunohistochemistry using an anti-SPP1
122 antibody demonstrated that SPP1 was localized in the cytoplasm of Langhans giant cells
123 (Figures 3 and 4), suggesting that these giant cells are a form of SPP1-positive
124 macrophages.

125 Additionally, CosMx™ spatial imaging and immunohistochemistry indicated that SPP1
126 was present in macrophages without giant cell morphology, located around
127 mycobacterium-positive granulomas in proximity to Langhans giant cells (Figure 3). This
128 observation implies that SPP1-positive macrophages initially infiltrate around the
129 granulomas, forming a barrier of macrophages, and that some of these cells may
130 subsequently fuse to form Langhans giant cells.

131 Bulk RNA-seq analysis of RNA extracted from mycobacterium-infected tissues also
132 revealed elevated expression of SPP1 in infected tissues compared to controls (Figures
133 5A-5C). Gene ontology analysis indicated that cytokine-mediated signaling pathways and
134 extracellular matrix organization were upregulated in mycobacterium-infected samples
135 (Figure 5D). These processes involved high expression of SPP1 and CD44, respectively.
136 Collectively, these findings suggest that SPP1-positive macrophages may play a critical
137 role in granuloma formation during mycobacterial infections.

138 **Ligand-receptor interaction of SPP1**

139 Using spatial transcriptome data, the R package InSituCor was employed for spatial
140 correlation analysis to detect significant ligand-receptor interactions in the samples. This
141 analysis identified SPP1, FN1, and MARCO as co-expression markers of SPP1-positive
142 macrophages (Figure 6A). Furthermore, InSituCor detected SPP1-CD44 and FN1-CD44
143 pairs as active ligand-receptor interactions in both NTM and MTB samples (Figures 6B-
144 C). Spatial imaging of these samples demonstrated that CD44-positive cells were
145 localized near SPP1-positive macrophages, though CD44-positive cells were distributed
146 more broadly compared to SPP1-positive macrophages. Spatial analysis also revealed co-
147 expression of CD44 and SPP1 in SPP1-positive macrophages (macrophage_d) of tissues
148 with mycobacterial infection (Figures 6D and 6E). Dot plot analysis showed that CD44

was expressed by a variety of cell types, including macrophages, mast cells, CD8+ T cells, and dendritic cells around the granulomatous lesions, while SPP1 expression was predominantly confined to the macrophage_d subtype (Figure 7A). Immunohistochemistry for SPP1 and CD44 showed SPP1 and CD44 expression in Langhans giant cells and various cells around SPP1-positive macrophages, respectively (Figure 7B). Spatial images of CosMx™ confirmed that CD44 was expressed not only in macrophages but also in various cell types, including B cells, T cells, and epithelial cells surrounding SPP1-positive macrophages (Figure 7C). The SPP1-CD44 interaction was also identified using the CellChat package (Figure 8). SPP1, expressed by macrophage_d, was shown to interact with various cell types. Circle plots and heatmaps of the SPP1 signaling pathway network indicated that the receiver cells for the SPP1-CD44 signal included macrophage_d, macrophage_c, and occasionally CD8+ cytotoxic T cells, while the sender cell was macrophage_d (SPP1-positive macrophage) (Figures 8B, 8C, 8E, and 8G). The receiver cells of the SPP1-CD44 signaling pathway varied among samples (Figure 8C). Although macrophages were the primary receiver cells, B cells, CD8+ T cells, and alveolar epithelial cells also acted as receivers in certain cases. Beyond the SPP1-CD44 signaling pathway, other significant cell communication pathways identified by CellChat included collagen, MHC-I, MIF, FN1, integrin β2, PECAM1, and ICAM pathways (Figure 8D, Supplementary Figure 9). The incoming and outgoing interactions of the SPP1-CD44 pathway by macrophage_d were relatively strong among the cell types and other pathways in mycobacterium-infected tissues (Figures 8A, 8F, and 8G, Supplementary Figure 9). In the SPP1-CD44 signaling pathway, SPP1 expressed by macrophage_d communicated with macrophage_d itself, mast cells, and CD8+ T cells (Figures 8E-G and Supplementary Figure 9).

SPP1-positive macrophages in granuloma associated with non-mycobacterial infection

To determine whether SPP1-positive macrophages are associated with granulomatous diseases beyond mycobacterial infections, pathological samples from granulomatous lesions in patients with rheumatoid nodule (RN), granulomatosis with polyangiitis (GPA), sarcoidosis (SA), Aspergillus pneumonia (AP), and aspiration pneumonia (Aspi-P) were examined. Immunohistochemistry revealed that SPP1 was present in some foreign body giant macrophages surrounding the granulomatous lesions across all tested samples (Figure 9 and Supplementary Figure10). RNA-seq analysis of RNA extracted from these granulomatous samples demonstrated elevated expression of SPP1 in the granulomatous lesions, similar to the expression levels observed in mycobacterial infections, compared with control lung and tonsil samples (Figures 5A-5C). Expression of CD40L(CD154) and

CD40 pair, another Ligand-Receptor pair reported as activation in granulomatous diseases[15], did not show significant difference between granulomatous samples and controls (Figure 5B). Furthermore, immunohistochemistry revealed CD44 expression in SPP1-positive macrophages and neighboring cells within the lesions of GPA, SA, and RN (Figure 9A and 9B). Immunofluorescence imaging also demonstrated that a subset of SPP1-positive macrophages expressed CD44 (Figure 9C). These findings suggest that SPP1-positive macrophages are broadly associated with granulomatous diseases, and that the SPP1-CD44 interaction is observed commonly in granulomatous pathology.

DISCUSSION

A pivotal discovery in our study was the identification of multiple macrophage subtypes within the tissues of granulomatous diseases. Based on gene expression patterns, we identified at least four distinct macrophage cell types. Among these, SPP1-positive macrophages predominantly infiltrated the regions surrounding NTM- and MTB-positive granulomatous tissue. Additionally, we found that Langhans giant cells were a specialized form of these SPP1-positive macrophages. Notably, besides these giant cells, we observed a significant number of SPP1-positive macrophages that did not exhibit giant cell morphology, indicating a diverse range of morphologies for these cells.

Our spatial transcriptomics data demonstrated that at least 26 types of cells infiltrated the lungs with mycobacterial infection (Fig.1). Although the percentages of infiltrating cell types varied among samples, macrophages were one of the major cell types in all seven samples. Along with macrophages, T cells, B cells, plasma cells, and dendritic cells were also observed as major cell types. These cell populations are consistent with those reported in MTB and NTM tissues in previous studies [2-9]. Macrophages have been shown to be key player in granuloma formation [5,7,10]. Various macrophage subtypes infiltrate granulomas alongside T and B cells in mycobacterial infections, with M1/M2 macrophage polarization inducing NF-kappa B activation, which is associated with granuloma formation and outcome[10].

SPP1, also known as osteopontin, is a multifunctional secreted phosphorylated glycoprotein produced by macrophages and T cells. It is associated with bone remodeling, T cell and B cell activation, and chemotaxis[16-20]. SPP1 expression in foreign body macrophages, such as Langhans giant cells, has been previously reported in pathological samples from tuberculosis and sarcoidosis [16,21-24]. Recent studies using single cell transcriptomics and/or spatial omics assay have highlighted the potential role of SPP1-positive macrophages in infections, inflammatory diseases, and cancer [25,26]. For instance,

221 in tissue samples from a patient with granulomatous slack skin, CD11c+/LYZ+
222 macrophages exhibited an M1-like phenotype and strongly expressed MMP9, MMP12,
223 CHI3L1, CHIT1, COL1A1, TIMP1, and SPP1, all of which are involved in extracellular
224 matrix degradation and tissue remodeling [27]. SPP1-positive macrophages have also been
225 detected in bronchoalveolar lavage fluid from tuberculosis patients [28]. Interestingly,
226 plasma osteopontin levels are higher in patients with tuberculosis and sarcoidosis
227 compared to healthy donors [29,30]. A study on perivascular adipose tissue in heart transplant
228 recipients demonstrated the presence of SPP1-positive macrophages in the perivascular
229 tissues, with an identified interaction between secreted SPP1 and CD44 [31]. These data
230 suggest that SPP1-positive macrophages secrete SPP1 and induce SPP1-CD44 signaling
231 in inflammation. In a *Schistosoma mansoni* egg-induced granuloma animal model,
232 granulomas from osteopontin-knockout animals were smaller and contained significantly
233 fewer macrophages, as well as fewer macrophage-derived epithelioid cells and giant cells
234 [32]. Thus, the presence of SPP1-positive macrophages in granulomatous tissues suggests
235 an important role for SPP1 in granuloma formation through its interactions.
236 In our study, we demonstrated that the SPP1-CD44 pathway was one of the main ligand-
237 receptor pairs involved in cell-cell communication in granulomatous lesions (Fig. 8A-
238 8D). Recent studies have shown that SPP1 is associated with cancer cell growth and
239 resistance to chemoradiotherapy, inducing epithelial-mesenchymal transition, autophagy,
240 aberrant glucose metabolism, epigenetic alterations, and reduced drug uptake through the
241 SPP1-CD44 signaling [33]. SPP1-positive macrophages have been identified in colorectal
242 cancer and squamous cell carcinoma[34,35]. In hepatocellular cancer, SPP1-positive
243 macrophages infiltrated hypoxic tumor regions with cancer stem cells, where the SPP1
244 signaling pathway was highly active in cell-cell communication with SPP1-CD44 and
245 SPP1-ITGA/ITGB identified as the main ligand-receptor pairs [36]. SPP1 also binds to
246 integrins α4β1, α9β1, and α9β4, inducing cell adhesion and migration. CD44 has also
247 been identified as a receptor for SPP1, and the SPP1-CD44 signaling pathway has been
248 reported in various cancers[37-39]. SPP1-positive macrophages have been detected in
249 cancers as tumor-associated macrophages, and the SPP1-CD44 pathway has been
250 identified as a critical mediator of communication between tumor-associated macrophage
251 subpopulations [40-42]. The SPP1-CD44 pathway has been linked to cancer chemoresistance
252 in solid tumors and to cell-to-cell communication between cancer cells and tumor-
253 associated macrophages [36,43,44]. The presence of SPP1-positive macrophages in cancers
254 correlates with worse prognosis and poor immunotherapy response, leading to reduced
255 survival [36,40]. Some therapeutic approaches targeting SPP1-CD44 signaling have been
256 reported in vitro and in vivo. In a mouse model, SPP1 was shown to induce cancer cell

257 chemoresistance by activating the CD44 receptor, and that treatment with anti-SPP1 and
258 anti-CD44 antibodies improved cancer cell sensitivity to cisplatin [45]. Importantly, the
259 SPP1-CD44 signaling pathway has been identified as a potential immune checkpoint
260 target[46,47]. CD44 expression in tumor cells was positively correlated with PD-L1
261 expression and the numbers of infiltrated CD68- and CD168-positive macrophages[48]. It
262 was also demonstrated that SPP1-CD44 immune checkpoint regulates CD8+ T cell
263 activation and tumor immune evasion in interferon regulatory factor 8 deficient mice [46].
264 Inhibition of the SPP1-CD44 pathway, therefore, may be a potential therapeutic strategy
265 to reduce granuloma formation in granulomatous diseases, such as mycobacterial
266 infections. In tuberculosis and MAC infections, granulomas encapsulate mycobacteria in
267 necrotic tissue to prevent their spread. Since granuloma formation is a major characteristic
268 of mycobacterial infections, further studies will be required to explore the inhibition of
269 the SPP1-CD44 pathway in macrophages.
270 In conclusion, our study sheds light on the intricate cellular dynamics involved in
271 granuloma formation in mycobacterial diseases. The prominence of SPP1-positive
272 macrophages, including Langhans giant cells, suggests that these cells may play a key
273 role in this process, opening avenues for further research and potential therapeutic
274 interventions.
275
276 **MATERIALS AND METHODS**
277 **Tissue samples**
278 Formalin-fixed paraffin embedded (FFPE) samples of resected lung tissues from patients
279 with active mycobacterial diseases, granulomatous diseases, or other controls were used
280 (S Table 1). For CosMx™ SMI analysis[14], 7 lung resections were obtained from 3 MTB
281 and 4 NTM patients undergoing lung resection surgery. Total 28 lung tissues from 25
282 patients were applied to histological analysis, immunohistochemistry and RNAseq
283 analysis by next generation sequencing. In addition, five intact lung tissues from patients
284 with cancer and four tonsillar tissues were used as controls. All MTB and NTM were
285 diagnosed as active disease by sputum culture and/or PCR method. The study was
286 approved by the Ethics Committee of National Institute of Infectious Diseases (approval
287 no. 1781) and National Hospital Organization Tokyo National Hospital (approval no. 408).
288
289 **CosMx™ spatial molecular imaging (SMI)**
290 CosMx™ Human Universal Cell Characterization RNA Panel (1000-plex; Nanostring,
291 Seattle, WA) was applied to 7 FFPE samples: 3 tuberculosis, 3 MAC-positive pneumonia,
292 and 1 MAC-negative bronchiectasis samples with 15-45 fields of view (FoVs) per sample

293 (216 total FoVs) (Supplementary Table 2). The mean area explored was 4.60 mm^2 per
294 sample. FOVs were placed on the tissue to match regions of interest identified by H&E
295 staining of an adjacent serial section. FoVs were selected from areas around granuloma
296 or inflammatory cell infiltration to avoid granulomatous necrotic tissues. Sample
297 preparation and CosMx™ SMI instrument run was performed as described previously
298 [14,25]. In addition to RNA readout, tissue samples were incubated with a fluorophore-
299 conjugated antibody cocktail against CD298/B2M (488 nm), PanCK (532 nm), CD45
300 (594 nm), and either CD3 or CD68 (647 nm) proteins and DAPI stain. Cell segmentation,
301 assigning transcripts at the cell-level, and obtaining a transcript by cell count matrix were
302 performed as previously described [14,25]. Following total count normalization across all
303 detected cells, highly variable genes (HVGs) were identified. Then, principal component
304 analysis (PCA) was computed on the HVGs. Finally, uniform manifold approximation
305 and projection (UMAP) was performed on these data[14,25].
306
307 **Cell type annotation**
308 To identify subpopulation markers, we ran findMarkers (scran package, version 1.22.1)[49],
309 blocking by sample, considering HVGs only, and testing for positive log-fold changes.
310 The 100 top ranked genes were selected and passed to SingleR (version 1.8.1)[50].
311
312 **Co-expression and cellular communication assay**
313 Spatial correlation analysis such as co-expression and receptor-ligand assay was
314 performed in the CosMx™ dataset with a R package InSituCor [51]. InSituCor was run on
315 normalized count data, adjusted for the effects of cell type, tissue ID and single cell counts,
316 to uncover spatial correlations beyond those accounted for by these variables. Cellular
317 communication for cell types were also analyzed with CellChat (http://www.cellchat.org/).
318 In CellChat, to convert spatial transcriptomics data of CosMx™, conversion.factor = 0.18
319 was used for setting spatial factors. In function "computeCommunProb", contact.range =
320 50 and scale.distance = 20 were used.
321
322 **Bulk RNA-seq analysis of lung tissues**
323 Total RNA was extracted from FFPE samples (Supplementary Table 1, 5 MTB, 7 NTM,
324 12 granulomatous diseases including 2 RN, 3 AP, 3 GPA, 3 SA, and 1 Aspi-P, 4 control
325 lung, and 4 tonsils) with Quick-DNA/RNA FFPE Miniprep Kit (Zymo Research).
326 Barcoded RNA-seq library was established with NEBNext Ultra II RNA Library Prep Kit
327 for Illumina (New England BioLabs, Ipswich, MA) according to the manufacturer's
328 instructions. Libraries were subjected to pair-end sequencing (300 cycles) on a Nextseq

1000 platform (Illumina, San Diego, CA). Quality filtering, adapter trimming, and RNAseq analyzing was performed using CLC genomics workbench (version 23, Qiagen, Hilden, Germany). Homo sapience refseq GRCh38.p13 was used as a reference genome of RNA sequences. PCA, volcano blot, and box plots were performed using the R (version 4.3.1) statistics package with RStudio (version 2023.06.1+524). Gene ontology assay was performed in biojupies (https://maayanlab.cloud/biojupies/analyze/).

Immunohistochemistry (IHC) and immunofluorescence (IF)

Immunostaining was performed in the tissue sections of mycobacterial infection and other granulomatous diseases. Anti-SPP1 rabbit polyclonal antibody (HPA027541, Sigma-Aldrich, St. Louis, MO) and anti-CD44 mouse monoclonal antibody (UMAB134, OriGene Technologies, Rockville, MD) were used as primary antibodies. For the second and third phase immunostaining reagents, a biotinylated F(ab')2 fragment of rabbit anti-mouse immunoglobulin (Dako, Copenhagen, Denmark) and peroxidase-conjugated streptavidin (Dako) were used. 3-3'diaminobenzidine was used as a chromogen and the slides were counterstained with hematoxylin. Nuclear counterstaining was performed with DAPI on IF samples. Image acquisition was performed on virtual slide system (VS200, Evident, Tokyo, Japan).

Data availability

Bulk RNA-seq and CosMx™ SMI raw data generated in this study have been deposited in the GEO Omnibus database under accession code GSE276060 and GSE276083, respectively. Seurat object, Giotto object, and DEG gene list (marker_heatmap_nb_clus_4.csv) are registered in figshare (https://figshare.com/).

Code availability

Full code for analysis of CosMx™ SMI data can be found at https://github.com/katanoh/Lung_CosMx_analysis.

Conflict of Interest

The authors declare that they have no conflict of interest.

Acknowledgment

The authors thank Mike McKenna, Claire Williams, Patrick Danaher, Joseph M. Beechem, Nanostring USA, Fumiyo Kurokawa, Takayuki Taniya, and Takashi Uematsu, Nanostring Japan, and Ikuyo Yamamoto, Department of Pathology, National Institute of Infectious

Diseases, for technical supports. The authors also thank Akiko Yamashita, Yukari Nogi, and Ginko Kaneda, Department of Mycobacteriology, National Institute of Infectious Diseases, for their assistance. This study was supported in part by grants from the Japan Agency for Medical Research and Development (AMED) to HK (JP24fk0108701) and to YH (JP23fk0108608, JP24fk0108673, JP24gm1610003, JP24gm1610007, JP24wm0125007, JP24wm0225022, JP24wm0325054, and JP24fk0108701). This study was also supported in part by grants from the Japan Society for the Promotion of Science (JSPS) for International Collaborative Research to YH (JP63KK0138), and for Scientific Research (A) to YH (JP24H00331), and for Scientific Research (C) to YH (JP23K07665 and 23K07958).

References

1 Furin, J., Cox, H. & Pai, M. Tuberculosis. *Lancet* **393**, 1642-1656, (2019).

2 Hunter, R. L. Pathology of post primary tuberculosis of the lung: an illustrated critical review. *Tuberculosis (Edinb)* **91**, 497-509, (2011).

3 Ulrichs, T. & Kaufmann, S. H. New insights into the function of granulomas in human tuberculosis. *J Pathol* **208**, 261-269, (2006).

4 Ehlers, S. & Schaible, U. E. The granuloma in tuberculosis: dynamics of a host-pathogen collusion. *Front Immunol* **3**, 411, (2012).

5 Russell, D. G., Cardona, P. J., Kim, M. J., Allain, S. & Altare, F. Foamy macrophages and the progression of the human tuberculosis granuloma. *Nat Immunol* **10**, 943-948, (2009).

6 Carow, B. *et al.* Immune mapping of human tuberculosis and sarcoidosis lung granulomas. *Front Immunol* **14**, 1332733, (2023).

7 Marakalala, M. J. *et al.* Inflammatory signaling in human tuberculosis granulomas is spatially organized. *Nat Med* **22**, 531-538, (2016).

8 Park, H. E. *et al.* Modulating macrophage function to reinforce host innate resistance against Mycobacterium avium complex infection. *Front Immunol* **13**, 931876, (2022).

9 Lin, P. L. *et al.* Sterilization of granulomas is common in active and latent tuberculosis despite within-host variability in bacterial killing. *Nat Med* **20**, 75-79, (2014).

10 Marino, S. *et al.* Macrophage polarization drives granuloma outcome during Mycobacterium tuberculosis infection. *Infect Immun* **83**, 324-338, (2015).

11 Smith, D., Hansch, H., Bancroft, G. & Ehlers, S. T-cell-independent granuloma formation in response to Mycobacterium avium: role of tumour necrosis factor-

401 alpha and interferon-gamma. *Immunology* **92**, 413-421, (1997).
402 12 Murray, P. J. Macrophage Polarization. *Annu Rev Physiol* **79**, 541-566, (2017).
403 13 Yoshida, M. *et al.* Transcriptome analysis of long non-coding RNAs in
404 Mycobacterium avium complex-infected macrophages. *Front Immunol* **15**,
405 1374437, (2024).
406 14 He, S. *et al.* High-plex imaging of RNA and proteins at subcellular resolution in
407 fixed tissue by spatial molecular imaging. *Nat Biotechnol* **40**, 1794-1806, (2022).
408 15 Villeneuve, J. *et al.* A Role for CD154, the CD40 Ligand, in Granulomatous
409 Inflammation. *Mediators Inflamm* **2017**, 2982879, (2017).
410 16 O'Regan, A. W. *et al.* Osteopontin is associated with T cells in sarcoid granulomas
411 and has T cell adhesive and cytokine-like properties in vitro. *J Immunol* **162**,
412 1024-1031, (1999).
413 17 Choi, S. T. *et al.* Osteopontin might be involved in bone remodelling rather than
414 in inflammation in ankylosing spondylitis. *Rheumatology (Oxford)* **47**, 1775-1779,
415 (2008).
416 18 Reinholt, F. P., Hultenby, K., Oldberg, A. & Heinegard, D. Osteopontin--a
417 possible anchor of osteoclasts to bone. *Proc Natl Acad Sci U S A* **87**, 4473-4475,
418 (1990).
419 19 Wang, K. X. & Denhardt, D. T. Osteopontin: role in immune regulation and stress
420 responses. *Cytokine Growth Factor Rev* **19**, 333-345, (2008).
421 20 Koh, A. *et al.* Role of osteopontin in neutrophil function. *Immunology* **122**, 466-
422 475, (2007).
423 21 Carlson, I., Tognazzi, K., Manseau, E. J., Dvorak, H. F. & Brown, L. F.
424 Osteopontin is strongly expressed by histiocytes in granulomas of diverse etiology.
425 *Lab Invest* **77**, 103-108, (1997).
426 22 Tsai, A. T. *et al.* The role of osteopontin in foreign body giant cell formation.
427 *Biomaterials* **26**, 5835-5843, (2005).
428 23 Nau, G. J. *et al.* A chemoattractant cytokine associated with granulomas in
429 tuberculosis and silicosis. *Proc Natl Acad Sci U S A* **94**, 6414-6419, (1997).
430 24 Wang, D. *et al.* The association between osteopontin and tuberculosis: A
431 systematic review and meta-analysis. *PLoS One* **15**, e0242702, (2020).
432 25 Garrido-Trigo, A. *et al.* Macrophage and neutrophil heterogeneity at single-cell
433 spatial resolution in human inflammatory bowel disease. *Nat Commun* **14**, 4506,
434 (2023).
435 26 MacDonald, L. *et al.* COVID-19 and RA share an SPP1 myeloid pathway that
436 drives PD-L1+ neutrophils and CD14+ monocytes. *JCI Insight* **6**, (2021).

27 Feng, Y. *et al.* Spatial transcriptomics reveals heterogeneity of macrophages in the tumor microenvironment of granulomatous slack skin. *J Pathol* **261**, 105-119, (2023).

28 Yang, Q. *et al.* The interaction of macrophages and CD8 T cells in bronchoalveolar lavage fluid is associated with latent tuberculosis infection. *Emerg Microbes Infect* **12**, 2239940, (2023).

29 Koguchi, Y. *et al.* High plasma osteopontin level and its relationship with interleukin-12-mediated type 1 T helper cell response in tuberculosis. *Am J Respir Crit Care Med* **167**, 1355-1359, (2003).

30 Kadota, J. *et al.* High plasma concentrations of osteopontin in patients with interstitial pneumonia. *Respir Med* **99**, 111-117, (2005).

31 Fu, M. *et al.* Single-Cell RNA Sequencing of Coronary Perivascular Adipose Tissue From End-Stage Heart Failure Patients Identifies SPP1(+) Macrophage Subpopulation as a Target for Alleviating Fibrosis. *Arterioscler Thromb Vasc Biol* **43**, 2143-2164, (2023).

32 O'Regan, A. W. *et al.* Abnormal pulmonary granuloma formation in osteopontin-deficient mice. *Am J Respir Crit Care Med* **164**, 2243-2247, (2001).

33 Kretschmer, C. *et al.* Identification of early molecular markers for breast cancer. *Mol Cancer* **10**, 15, (2011).

34 Bill, R. *et al.* CXCL9:SPP1 macrophage polarity identifies a network of cellular programs that control human cancers. *Science* **381**, 515-524, (2023).

35 Qi, J. *et al.* Single-cell and spatial analysis reveal interaction of FAP(+) fibroblasts and SPP1(+) macrophages in colorectal cancer. *Nat Commun* **13**, 1742, (2022).

36 Fan, G. *et al.* Single-cell and spatial analyses revealed the co-location of cancer stem cells and SPP1+ macrophage in hypoxic region that determines the poor prognosis in hepatocellular carcinoma. *NPJ Precis Oncol* **8**, 75, (2024).

37 Weber, G. F., Ashkar, S., Glimcher, M. J. & Cantor, H. Receptor-ligand interaction between CD44 and osteopontin (Eta-1). *Science* **271**, 509-512, (1996).

38 Liu, L. *et al.* Construction of TME and Identification of crosstalk between malignant cells and macrophages by SPP1 in hepatocellular carcinoma. *Cancer Immunol Immunother* **71**, 121-136, (2022).

39 Wang, C. *et al.* The heterogeneous immune landscape between lung adenocarcinoma and squamous carcinoma revealed by single-cell RNA sequencing. *Signal Transduct Target Ther* **7**, 289, (2022).

40 Xu, L. *et al.* Tumor-associated macrophage subtypes on cancer immunity along with prognostic analysis and SPP1-mediated interactions between tumor cells and

macrophages. *PLoS Genet* **20**, e1011235, (2024).

41 He, H. *et al.* Multi-dimensional single-cell characterization revealed suppressive immune microenvironment in AFP-positive hepatocellular carcinoma. *Cell Discov* **9**, 60, (2023).

42 He, C. *et al.* Single-Cell Transcriptomic Analysis Revealed a Critical Role of SPP1/CD44-Mediated Crosstalk Between Macrophages and Cancer Cells in Glioma. *Front Cell Dev Biol* **9**, 779319, (2021).

43 Xie, W. *et al.* Multi-Transcriptomic Analysis Reveals the Heterogeneity and Tumor-Promoting Role of SPP1/CD44-Mediated Intratumoral Crosstalk in Gastric Cancer. *Cancers (Basel)* **15**, (2022).

44 Nallasamy, P. *et al.* Pancreatic Tumor Microenvironment Factor Promotes Cancer Stemness via SPP1-CD44 Axis. *Gastroenterology* **161**, 1998-2013 e1997, (2021).

45 Qian, J. *et al.* Cancer-associated mesothelial cells promote ovarian cancer chemoresistance through paracrine osteopontin signaling. *J Clin Invest* **131**, (2021).

46 Klement, J. D. *et al.* An osteopontin/CD44 immune checkpoint controls CD8+ T cell activation and tumor immune evasion. *J Clin Invest* **128**, 5549-5560, (2018).

47 Lu, C. *et al.* WDR5-H3K4me3 epigenetic axis regulates OPN expression to compensate PD-L1 function to promote pancreatic cancer immune escape. *J Immunother Cancer* **9**, (2021).

48 Liu, S. *et al.* CD44 is a potential immunotherapeutic target and affects macrophage infiltration leading to poor prognosis. *Sci Rep* **13**, 9657, (2023).

49 Haghverdi, L., Lun, A. T. L., Morgan, M. D. & Marioni, J. C. Batch effects in single-cell RNA-sequencing data are corrected by matching mutual nearest neighbors. *Nat Biotechnol* **36**, 421-427, (2018).

50 Aran, D. *et al.* Reference-based analysis of lung single-cell sequencing reveals a transitional profibrotic macrophage. *Nat Immunol* **20**, 163-172, (2019).

51 Danaher, P. *et al.* Single cell spatial transcriptomic profiling of childhood-onset lupus nephritis reveals complex interactions between kidney stroma and infiltrating immune cells. *bioRxiv*, (2023).

505 **Figure legends**

506 **Figure 1.** Single cell analysis of CosMx™ in mycobacterium-infected tissues. A.
507 Overview of the study design for CosMx™ SMI, RNA-seq, and histological analysis.
508 Lung samples including MTB, NTM, granulomatous diseases and controls were
509 processed using RNA-seq (n = 37 samples) and CosMx™ SMI (n = 7 samples). This
510 figure was created with BioRender.com. B. Heatmap of gene expression and cell types
511 based on single cell data from CosMx™. C. Dot plots showing expression of cell-typing
512 markers in the indicated cell clusters. The dot size represents the percentage of cells
513 expressing the genes in each cluster. The average expression intensity of the markers is
514 shown using blue/red color. D. UMAP plots of 300,841 cells from lung tissues with 4
515 NTM or 3 MTB patients. Each cluster is shown in a different color. E. Stacked bar graph
516 showing the distribution of cell types across 7 tissue samples.

517

518 **Figure 2.** Subtyping of macrophages. A. Violin plot showing macrophage-associated
519 protein expression in macrophages and dendritic cells. B. Dot plot illustrating
520 macrophage-associated protein expression specially in macrophages. C. UMAP plot
521 depicting four macrophage subtypes. D. UMAP plot displaying the expression of
522 macrophage-associated proteins.

523

524 **Figure 3**. Spatial images of SPP1-positive macrophages (macrophage_d) in MAC-
525 positive lung tissues (Case NTM2). A. HE staining (left panel), immunofluorescence
526 (second panel), and CosMx™ spatial images (right two panels) of macrophage_d. Colors
527 representing different cell types are shown in the right panel. In CosMx™ images, SPP1
528 and MARCO signals are indicated by green and red dots, respectively. B. Enlarged images
529 of the boxed regions in A. C. Immunohistochemistry for SPP1 in the same tissue near the
530 granuloma.

531

532 **Figure 4**. CosMx™ spatial images of SPP1 and MARCO expression in macrophage_d in
533 MTB tissue (Case MTB1). A. Macrophage_d in the interstitial region expressed SPP1
534 and MARCO. B. Enlarged images of the boxed regions in A. C. Immunohistochemistry
535 for SPP1 in the same tissue near the granuloma.

536

537 **Figure 5**. RNAseq Results for granulomatous diseases and mycobacterial infection. A.
538 Principal component analysis (PCA) of RNAseq data for 37 samples. B. Volcano plot
539 comparing granulomatous diseases (granulomatous diseases and mycobacterial
540 infections) versus control groups. The expression of SPP1, FN1, and MARCO is

541 significantly higher in the granulomatous disease group. C. Box plot showing SPP1, FN1,
542 and MARCO expression in control lung (CTL-Lung, n=5), granulomatous diseases
543 (Granul, n=12), and the mycobacterial infection group (MTB+NTM, Mycob, n=16).
544 Transcripts per million (TPM) values for each gene are plotted. P values are displayed on
545 comparison lines. An asterisk (*) indicates a significant difference. D. Gene Ontology
546 analysis comparing mycobacterial infection tissues to control lungs, with upregulated
547 pathways listed in the left panel.
548
549 **Figure 6.** Coexpression and ligand-receptor assay in InSituCor. A. Heatmap of
550 coexpressed transcripts across different cell types. Coexpression of FN1, SPP1, and
551 MARCO was specifically observed in macrophage_d (highlighted by the broken red line).
552 B. Conditional correlation of ligand-receptor pairs in the ligand-receptor assay. The SPP1-
553 CD44 and FN1-CD44 pairs show strong conditional correlations. C. Correlation network
554 of SPP1 and CD44-associated transcripts. D. Spatial images showing SPP1-CD44
555 correlations in MTB and NTM tissues. Yellow indicates high correlation in the images
556 (left: MTB1, right: NTM2). E. Spatial images from CosMx™ analysis of MTB and NTM
557 samples. High expression of SPP1, CD44, and both are indicated by yellow, blue, and red
558 dots, respectively.
559
560 **Figure 7**. Expression of SPP1 and CD44 in macrophages around granuloma tissue with
561 mycobacterial infection. A. Dot plot showing the expression of SPP1, MARCO, FN1, and
562 CD44 across all cell types. B. Immunohistochemistry for SPP1 and CD44 in tissues from
563 patients with MTB (upper panels) and NTM (lower panels) infections. C.
564 Immunofluorescence and CosMx™ spatial images for SPP1 and CD44. SPP1 was
565 expressed in the cytoplasm of multinuclear giant cells (immunofluorescence assay, left
566 panels). CD44 expression was observed on the membrane of multinucleated giant cells
567 and their neighboring cells. CosMx™ spatial images (right panels) showed that
568 macrophage_d expresses both SPP1 and CD44. Colors representing different cell types
569 are shown in the bottom right panel.
570
571 **Figure 8**. Analysis of cellular communication among cell types using CellChat. A and B.
572 Circular plots showing interactions among cell types in all pathways (A) and specifically
573 in the SPP1 signaling pathway (B) across all seven cases analyzed with CosMx™. C.
574 Circular plots depicting interactions among cell types in the SPP1 signaling pathway in
575 each individual case. D. Histogram showing the relative contribution of each ligand-
576 receptor (L-R) pair across all seven cases analyzed with CosMx™. Only significant L-R

577 pairs are shown, with SPP1 interacting exclusively with CD44. E. Heatmap illustrating
578 the signal intensity of the sender and receiver in the SPP1 signaling pathway across all
579 samples. F. Dot plots showing the outgoing communication patterns of secreting cells.
580 Significant outgoing signals in the identified signaling pathways are represented by dots.
581 G. Dot plots showing the incoming communication patterns of secreting cells. Significant
582 incoming signals are represented by dots.
583
584 **Figure 9**. SPP1 and CD44 expression in tissues from patients with granulomatous
585 diseases. A. HE staining. B. Immunohistochemistry for SPP1. C. Immunofluorescence of
586 SPP1 and CD44. Tissues from patients with sarcoidosis (left), granulomatosis with
587 polyangiitis (GPA, middle), and rheumatoid nodule (RN, right) were investigated.
588
589

Fig.1

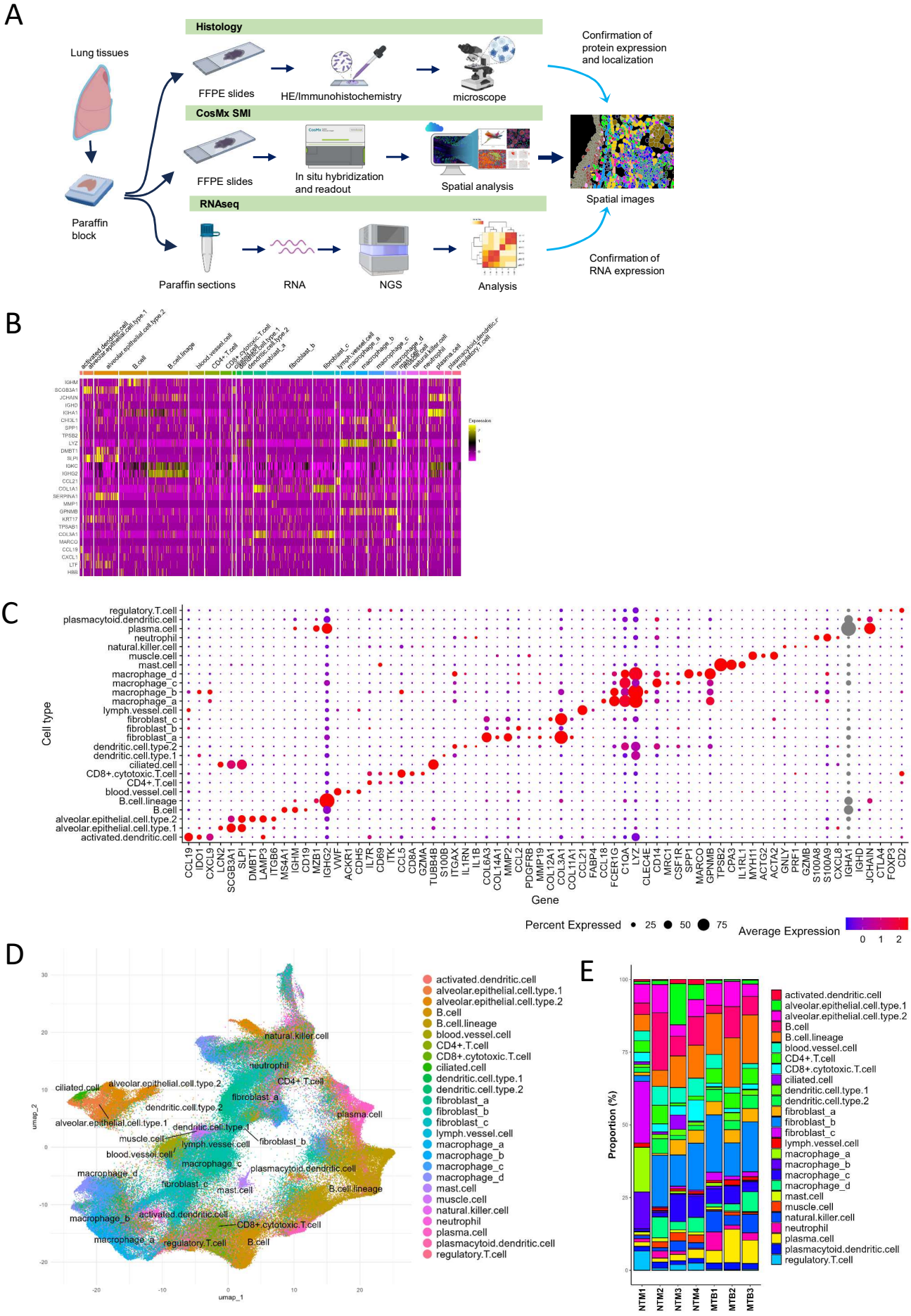
A
Lung tissues
Paraffin block
Histology
FFPE slides
HE/Immunohistochemistry
microscope
Confirmation of protein expression and localization
CosMx SMI
FFPE slides
In situ hybridization and readout
Spatial analysis
Spatial images
RNAseq
Paraffin sections
RNA
NGS
Analysis
Confirmation of RNA expression
B
Expression
C
Cell type
Gene
Percent Expressed
Average Expression
D
umap_1
umap_2
E
Proportion (%)
NTM1
NTM2
NTM3
NTM4
MTB1
MTB2
MTB3

Fig.2

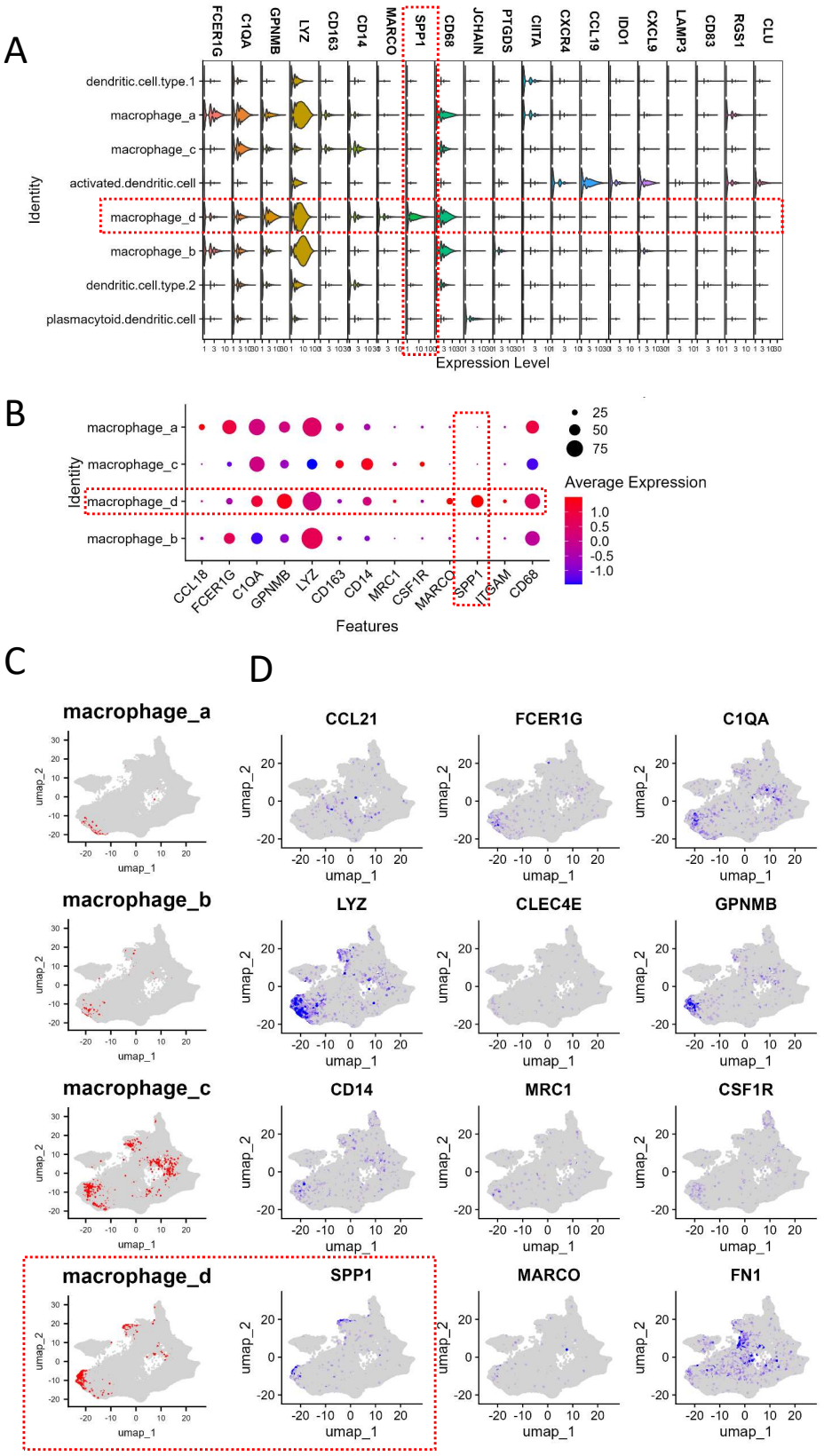
A
FCER1G
C1QA
GPNMB
LYZ
CD163
CD14
MARCO
SPP1
CD68
JCHAIN
PTGDS
CIITA
CXCR4
CCL19
IDO1
CXCL9
LAMP3
CD83
RGS1
CLU
dendritic.cell.type.1
macrophage_a
macrophage_c
activated.dendritic.cell
macrophage_d
macrophage_b
dendritic.cell.type.2
plasmacytoid.dendritic.cell
Identity
Expression Level
B
macrophage_a
macrophage_c
macrophage_d
macrophage_b
Identity
CCL18
FCER1G
C1QA
GPNMB
LYZ
CD163
CD14
MRC1
CSF1R
MARCO
SPP1
ITGAM
CD68
Features
25
50
75
Average Expression
1.0
0.5
0.0
-0.5
-1.0
C
D
macrophage_a
macrophage_b
macrophage_c
macrophage_d
CCL21
FCER1G
C1QA
LYZ
CLEC4E
GPNMB
CD14
MRC1
CSF1R
SPP1
MARCO
FN1
umap_1
umap_2

Fig.3

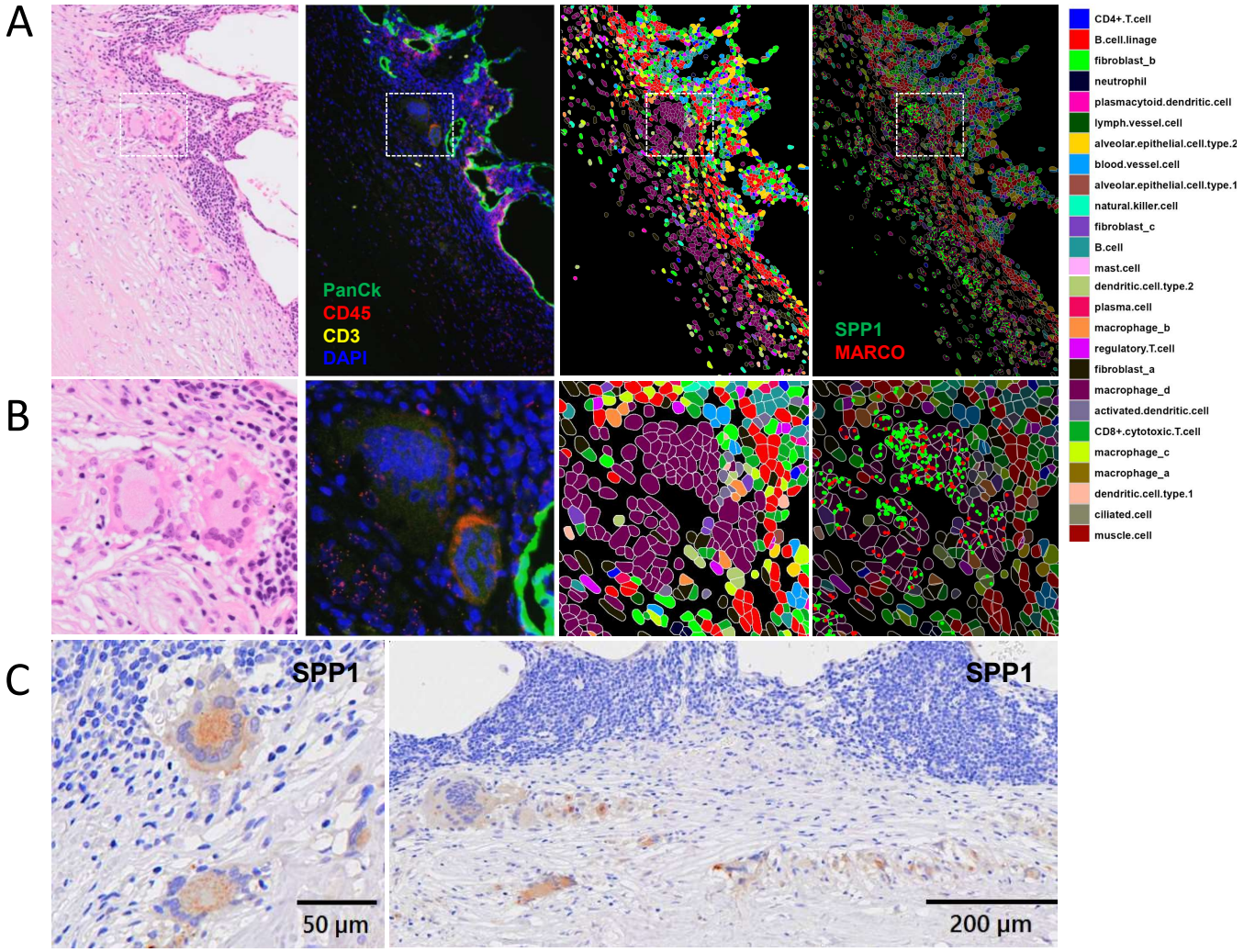
A
B
C
PanCk
CD45
CD3
DAPI
SPP1
MARCO
SPP1
50 μm
SPP1
200 μm
CD4+.T.cell
B.cell.linage
fibroblast_b
neutrophil
plasmacytoid.dendritic.cell
lymph.vessel.cell
alveolar.epithelial.cell.type.2
blood.vessel.cell
alveolar.epithelial.cell.type.1
natural.killer.cell
fibroblast_c
B.cell
mast.cell
dendritic.cell.type.2
plasma.cell
macrophage_b
regulatory.T.cell
fibroblast_a
macrophage_d
activated.dendritic.cell
CD8+.cytotoxic.T.cell
macrophage_c
macrophage_a
dendritic.cell.type.1
ciliated.cell
muscle.cell

Fig.4

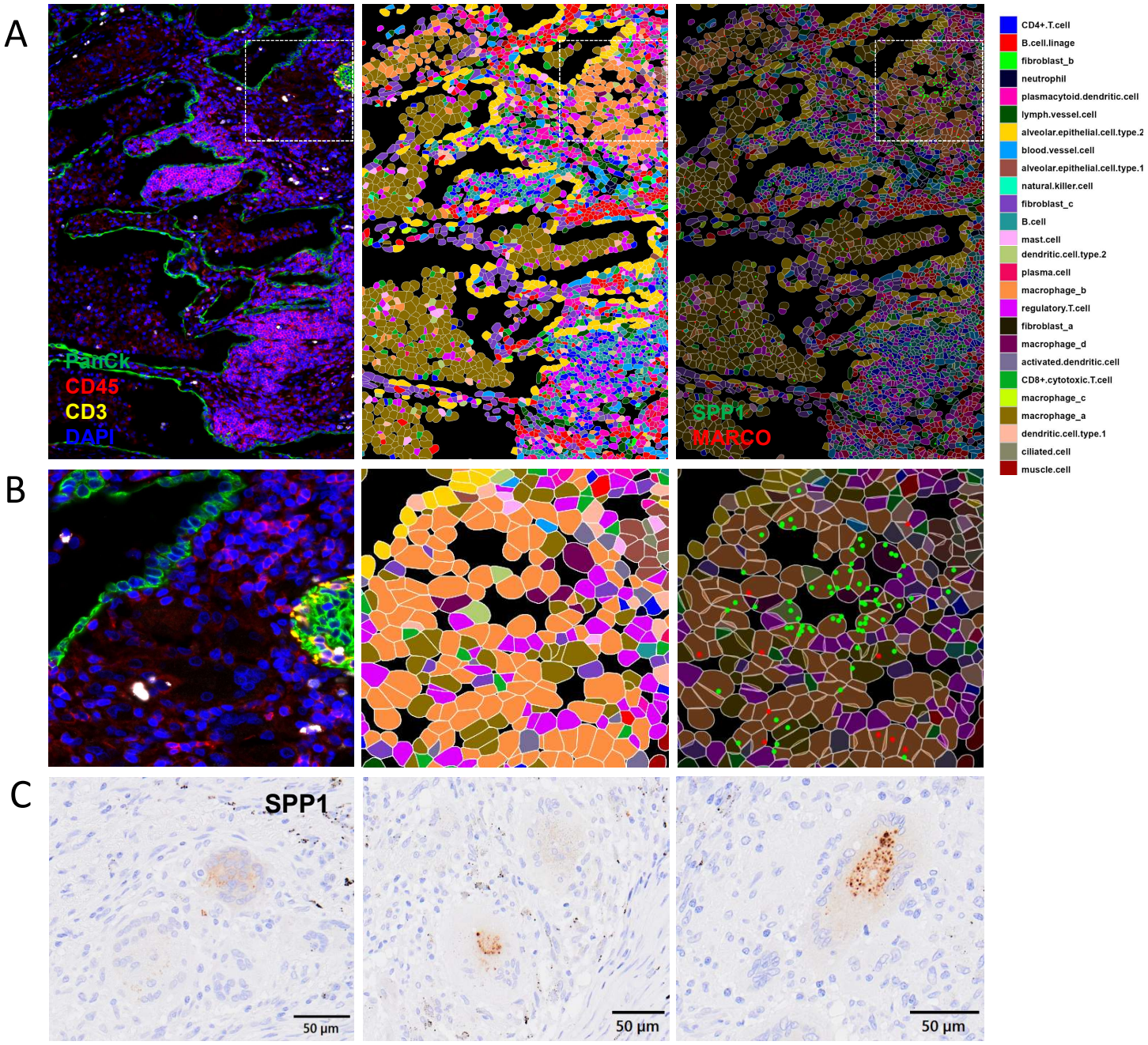
A
PanCk
CD45
CD3
DAPI
SPP1
MARCO
CD4+.T.cell
B.cell.linage
fibroblast_b
neutrophil
plasmacytoid.dendritic.cell
lymph.vessel.cell
alveolar.epithelial.cell.type.2
blood.vessel.cell
alveolar.epithelial.cell.type.1
natural.killer.cell
fibroblast_c
B.cell
mast.cell
dendritic.cell.type.2
plasma.cell
macrophage_b
regulatory.T.cell
fibroblast_a
macrophage_d
activated.dendritic.cell
CD8+.cytotoxic.T.cell
macrophage_c
macrophage_a
dendritic.cell.type.1
ciliated.cell
muscle.cell
B
C
SPP1
50 μm
50 μm
50 μm

Fig.5

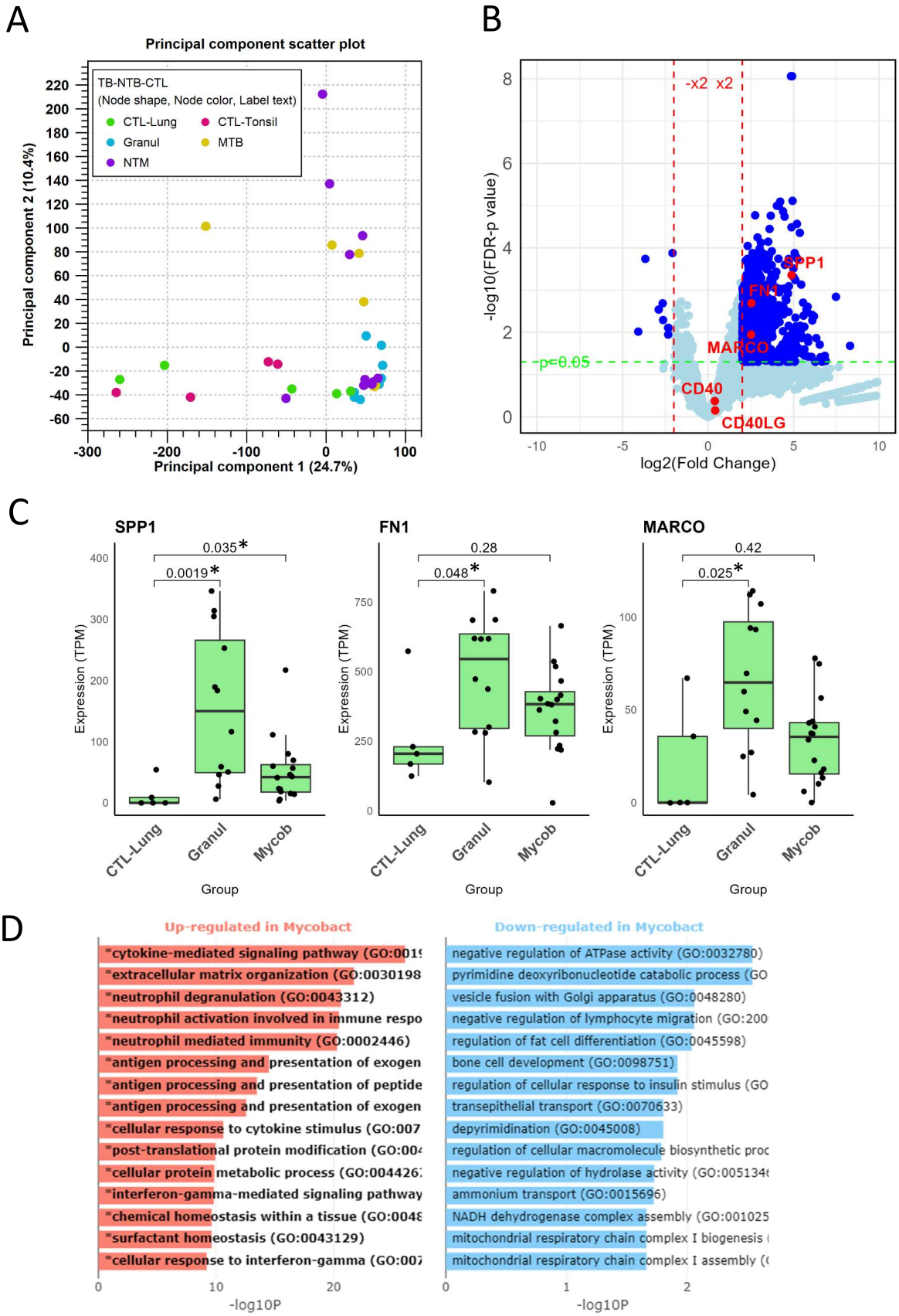
A
Principal component scatter plot
TB-NTB-CTL
(Node shape, Node color, Label text)
CTL-Lung
CTL-Tonsil
Granul
MTB
NTM
Principal component 2 (10.4%)
Principal component 1 (24.7%)
B
-x2 x2
SPP1
FN1
MARCO
CD40
CD40LG
p=0.05
-log10(FDR-p value)
log2(Fold Change)
C
SPP1
FN1
MARCO
0.035*
0.0019*
0.28
0.048*
0.42
0.025*
Expression (TPM)
CTL-Lung
Granul
Mycob
Group
D
Up-regulated in Mycobact
*cytokine-mediated signaling pathway (GO:001
*extracellular matrix organization (GO:0030198
*neutrophil degranulation (GO:0043312)
*neutrophil activation involved in immune respo
*neutrophil mediated immunity (GO:0002446)
*antigen processing and presentation of exogen
*antigen processing and presentation of peptide
*antigen processing and presentation of exogen
*cellular response to cytokine stimulus (GO:007
*post-translational protein modification (GO:00
*cellular protein metabolic process (GO:004426
*interferon-gamma-mediated signaling pathway
*chemical homeostasis within a tissue (GO:0048
*surfactant homeostasis (GO:0043129)
*cellular response to interferon-gamma (GO:007
-log10P
Down-regulated in Mycobact
negative regulation of ATPase activity (GO:0032780)
pyrimidine deoxyribonucleotide catabolic process (GO
vesicle fusion with Golgi apparatus (GO:0048280)
negative regulation of lymphocyte migration (GO:200
regulation of fat cell differentiation (GO:0045598)
bone cell development (GO:0098751)
regulation of cellular response to insulin stimulus (GO
transepithelial transport (GO:0070633)
depyrimidination (GO:0045008)
regulation of cellular macromolecule biosynthetic proc
negative regulation of hydrolase activity (GO:005134
ammonium transport (GO:0015696)
NADH dehydrogenase complex assembly (GO:001025
mitochondrial respiratory chain complex I biogenesis
mitochondrial respiratory chain complex I assembly
-log10P

Fig.6

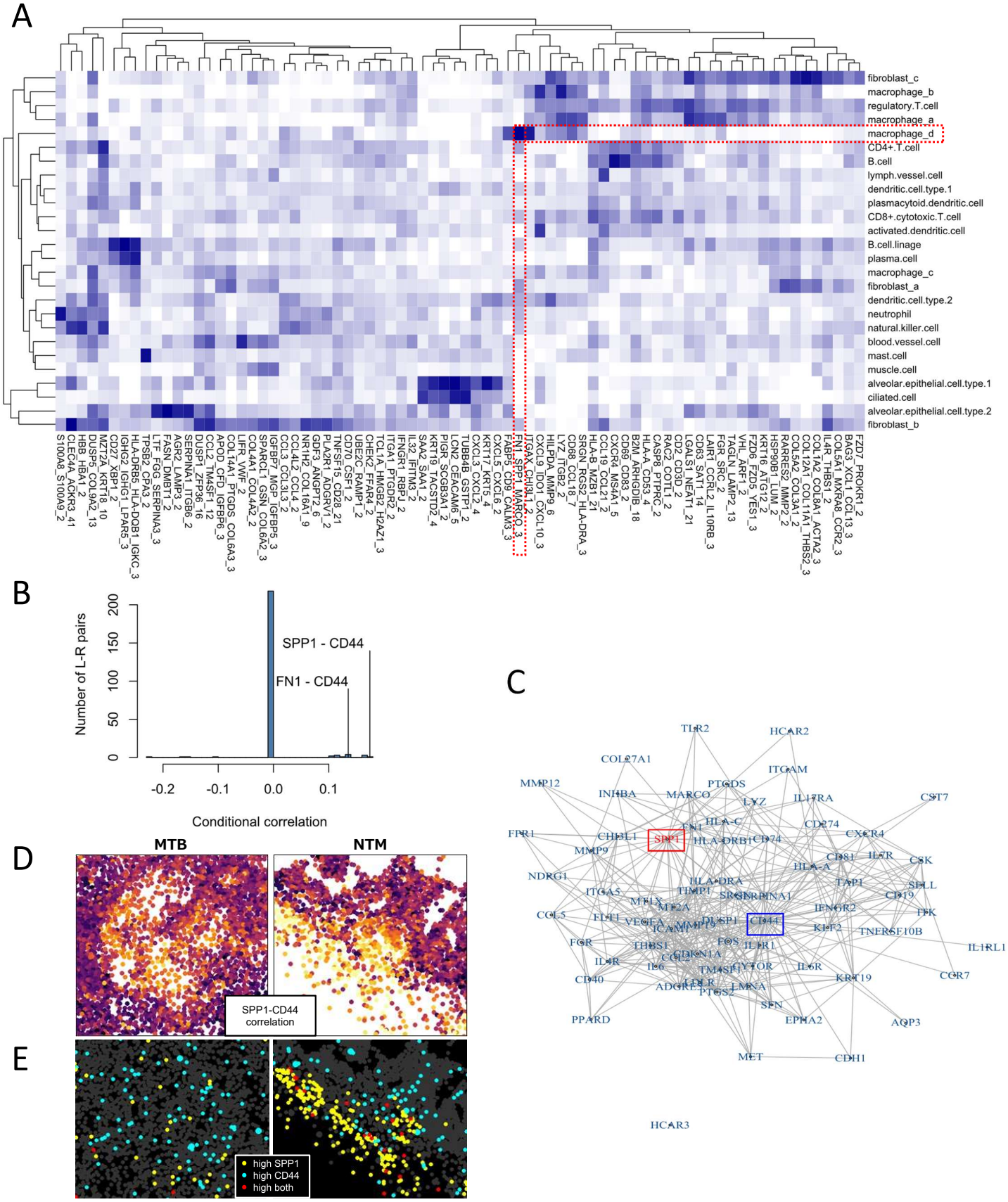
A
fibroblast_c
macrophage_b
regulatory.T.cell
macrophage_a
macrophage_d
CD4+.T.cell
B.cell
lymph.vessel.cell
dendritic.cell.type.1
plasmacytoid.dendritic.cell
CD8+.cytotoxic.T.cell
activated.dendritic.cell
B.cell.linage
plasma.cell
macrophage_c
fibroblast_a
dendritic.cell.type.2
neutrophil
natural.killer.cell
blood.vessel.cell
mast.cell
muscle.cell
alveolar.epithelial.cell.type.1
ciliated.cell
alveolar.epithelial.cell.type.2
fibroblast_b
B
Number of L-R pairs
SPP1 - CD44
FN1 - CD44
Conditional correlation
C
D
MTB
NTM
SPP1-CD44 correlation
E
high SPP1
high CD44
high both

Fig.7

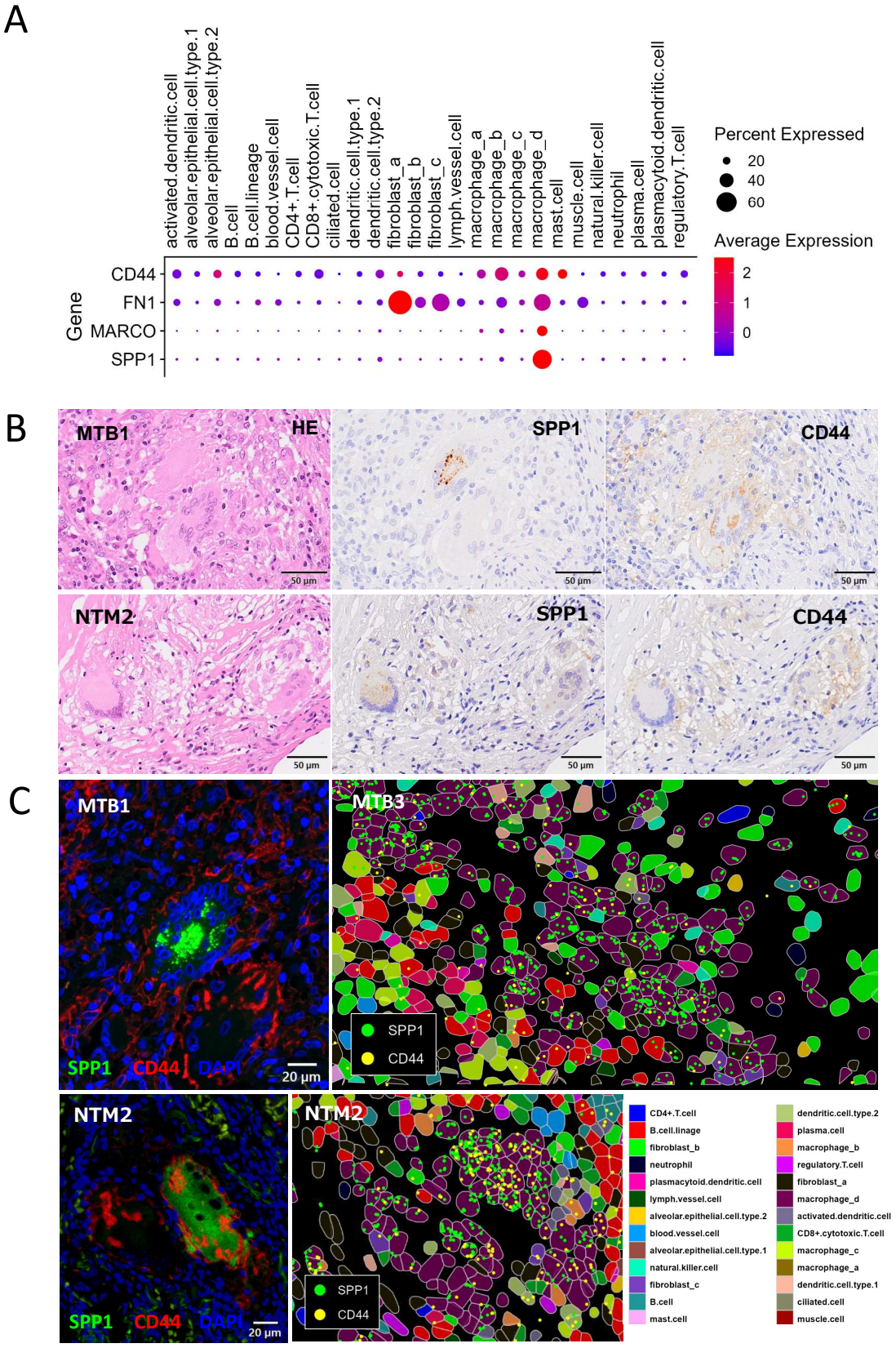
A
activated.dendritic.cell
alveolar.epithelial.cell.type.1
alveolar.epithelial.cell.type.2
B.cell
B.cell.linage
blood.vessel.cell
CD4+.T.cell
CD8+.cytotoxic.T.cell
ciliated.cell
dendritic.cell.type.1
dendritic.cell.type.2
fibroblast_a
fibroblast_b
fibroblast_c
lymph.vessel.cell
macrophage_a
macrophage_b
macrophage_c
macrophage_d
mast.cell
muscle.cell
natural.killer.cell
neutrophil
plasma.cell
plasmacytoid.dendritic.cell
regulatory.T.cell
Gene
CD44
FN1
MARCO
SPP1
Percent Expressed
20
40
60
Average Expression
2
1
0
B
MTB1
HE
SPP1
CD44
NTM2
50 μm
C
MTB1
SPP1
CD44
DAPI
20 μm
MTB3
NTM2
CD4+.T.cell
B.cell.linage
fibroblast_b
neutrophil
plasmacytoid.dendritic.cell
lymph.vessel.cell
alveolar.epithelial.cell.type.2
blood.vessel.cell
alveolar.epithelial.cell.type.1
natural.killer.cell
fibroblast_c
B.cell
mast.cell
dendritic.cell.type.2
plasma.cell
macrophage_b
regulatory.T.cell
fibroblast_a
macrophage_d
activated.dendritic.cell
CD8+.cytotoxic.T.cell
macrophage_c
macrophage_a
dendritic.cell.type.1
ciliated.cell
muscle.cell

Fig.8

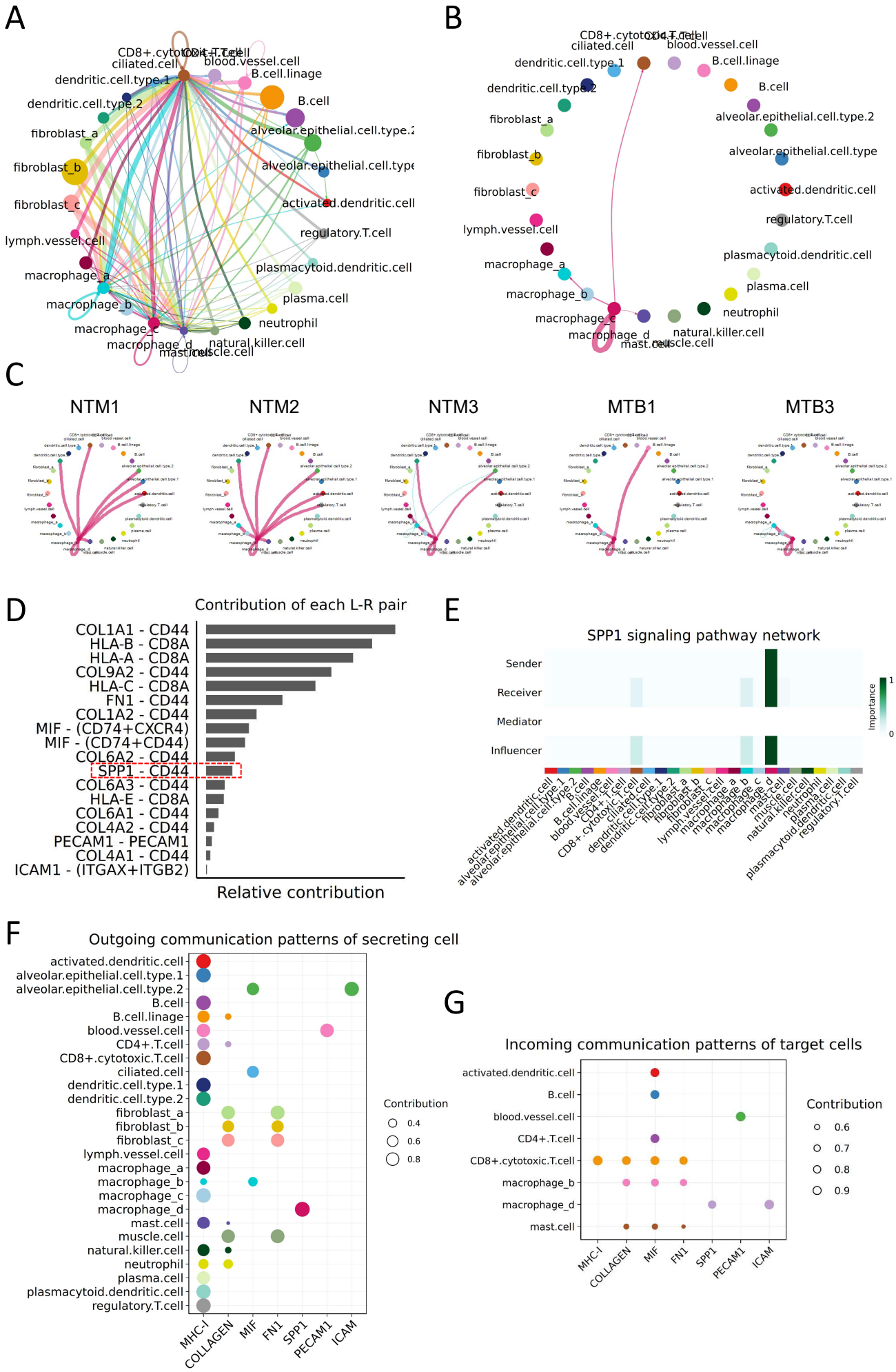
A
B
C
NTM1
NTM2
NTM3
MTB1
MTB3
D
Contribution of each L-R pair
COL1A1 - CD44
HLA-B - CD8A
HLA-A - CD8A
COL9A2 - CD44
HLA-C - CD8A
FN1 - CD44
COL1A2 - CD44
MIF - (CD74+CXCR4)
MIF - (CD74+CD44)
COL6A2 - CD44
SPP1 - CD44
COL6A3 - CD44
HLA-E - CD8A
COL6A1 - CD44
COL4A2 - CD44
PECAM1 - PECAM1
COL4A1 - CD44
ICAM1 - (ITGAX+ITGB2)
Relative contribution
E
SPP1 signaling pathway network
Sender
Receiver
Mediator
Influencer
Importance
F
Outgoing communication patterns of secreting cell
Contribution
MHC-I
COLLAGEN
MIF
FN1
SPP1
PECAM1
ICAM
G
Incoming communication patterns of target cells
Contribution

Fig.9

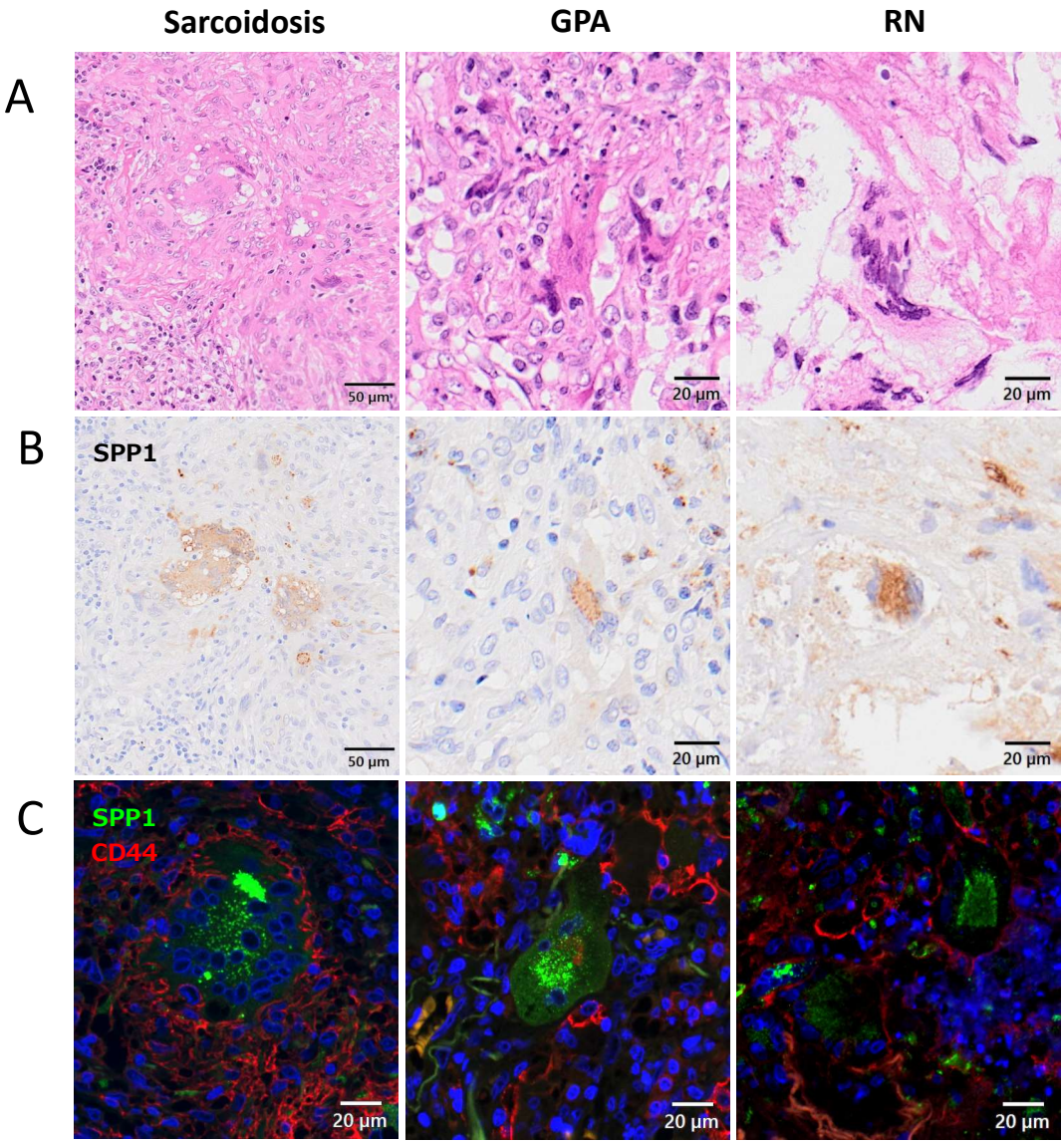
Sarcoidosis
GPA
RN
A
B
C
SPP1
SPP1
CD44
50 μm
20 μm
20 μm
50 μm
20 μm
20 μm
20 μm
20 μm
20 μm

Supplementary Data

Identification of SPP1-positive macrophages by single-cell spatial analysis in human lung tissues with mycobacterial infection

Harutaka Katano, Akira Hebisawa, Yuko Sato, Yoshihiko Hoshino

Supplementary Table 1: patient and sample list. AP: Aspergillus pneumonia, Aspi P: aspiration pneumonia, BCG: Bacille Calmette-Guerin, CTL: control, FFPE: formalin-fixed paraffin-embedded sample, GPA: granulomatosis with polyangiitis, IHC: immunohistochemistry, MAC: mycobacterium avium intracellulae complex, MTB: mycobacterium tuberculosis, NTM: non tuberculosis mycobacterium infection, ND: no data, RN: rheumatoid nodule, SA: sarcoidosis.

ID	Age	Gender	Group	Clinical diagnosis	BCG-IHC in FFPE	Real-time PCR in FFPE	CosMx
MTB1	49	M	MTB	MTB	+	MTB	MTB1
MTB2	70	M	MTB	MTB	+	MTB	MTB2
MTB3	64	M	MTB	MTB	+	MTB	MTB3
MTB4	38	M	MTB	MTB	-	MTB	
MTB5	49	M	MTB	MTB	-	-	
MTB6	49	M	MTB	MTB	-	MTB	
NTM1	71	M	NTM	NTM	+	MAC	NTM1
NTM2	56	F	NTM	NTM	+	MAC	NTM2
NTM3	63	F	NTM	NTM	+	MAC	NTM3
NTM4	51	F	NTM	NTM	-	-	NTM4
NTM5	51	F	NTM	NTM	-	-	
NTM6	51	F	NTM	NTM	+	M.Kansasii	
NTM7	66	F	NTM	NTM	+	MAC	
NTM8	66	F	NTM	NTM	+	MAC	
NTM9	73	M	NTM	NTM	-	MAC	
NTM10	68	F	NTM	NTM	-	-	
Ctl-Lung1	62	F	CTL-Lung	Lung cancer (control)	-	-	
Ctl-Lung2	63	M	CTL-Lung	Lung cancer (control)	-	-	
Ctl-Lung3	70	M	CTL-Lung	Lung cancer (control)	-	-	
Ctl-Lung4	80	M	CTL-Lung	Lung cancer (control)	-	-	
Ctl-Lung5	54	M	CTL-Lung	Lung cancer (control)	-	-	
Ctl-Tonsil1	ND	ND	CTL-Tonsil	tonsillitis (control)	-	-	
Ctl-Tonsil2	ND	ND	CTL-Tonsil	tonsillitis (control)	-	-	
Ctl-Tonsil3	ND	ND	CTL-Tonsil	tonsillitis (control)	-	-	
Ctl-Tonsil4	ND	ND	CTL-Tonsil	tonsillitis (control)	-	-	
Granulo1	70	M	Granulo	RN	-	-	
Granulo2	77	M	Granulo	RN	-	-	
Granulo3	50	M	Granulo	AP	-	-	
Granulo4	52	M	Granulo	AP	-	-	
Granulo5	69	F	Granulo	AP	-	-	
Granulo6	58	F	Granulo	GPA	-	-	
Granulo7	71	M	Granulo	GPA	-	-	
Granulo8	77	F	Granulo	GPA	-	-	
Granulo9	56	F	Granulo	SA	-	-	
Granulo10	37	F	Granulo	SA	-	-	
Granulo11	37	M	Granulo	SA	-	-	
Granulo12	62	M	Granulo	Aspi P	-	-	

Supplementary Table 2: Summary of CosMx assay on 7 slides of MTB and NTM samples. FOV: focus of view.

tissue	MTB1	MTB2	MTB3	NTM1	NTM2	NTM3	NTM4	Total	Mean
Number_of_FOVs	21	47	45	21	15	22	45	216	30.9
Total_Tissue_Area_mm2	8.33	4.65	4.16	3.63	2.09	4.28	5.08	32.2	4.6
Number_of_Cells_in_Final_Analysis	70649	40962	34799	31874	23692	51176	47689	300841	42977
Total_Transcripts_Assigned_to_Cells	8768373	7013069	4749647	4267383	1882347	5634413	7876583	40191815	5741688
Mean_Transcripts_per_Cell	124.1	171.2	136.5	133.9	79.5	110.1	165.2	920.5	131.5
Maximum_Transcripts_per_Cell	2226	2079	1697	2339	728	1362	2944	13375.0	1910.7
Mean_Unique_Genes_Per_Cell	70.14	65.82	58.73	81.5	54.69	69.42	79.18	479.5	68.5
Mean_Transcripts_per_um2	0.0357	0.0222	0.0178	0.0458	0.0323	0.0466	0.0228	0.2	0.0

Supplementary Table 3: Cell population in CosMx assay on 7 slides of MTB and NTM samples.

Cell types	MTB1	MTB2	MTB3	NTM1	NTM2	NTM3	NTM4	overall_ percentage
activated.dendritic.cell	0.71	0.15	0.25	0.36	1.75	0.34	1.46	0.72
alveolar.epithelial.cell.type.1	0.94	0.53	1.36	1.4	5.18	1.05	14.12	2.76
alveolar.epithelial.cell.type.2	6.48	8.67	4.26	9.7	5.88	7.49	3.95	6.72
B.cell	3.97	10.71	6.36	19.78	9.82	2.82	6.77	7.87
B.cell.lineage	5.63	17.05	16.73	5.54	11.32	14.11	10.89	11.19
blood.vessel.cell	3.38	2	1.62	6.5	6.13	4.81	5.28	4.16
CD4+.T.cell	3.98	5.24	5.39	6.38	1.4	5.09	0.97	4.07
CD8+.cytotoxic.T.cell	3.24	1.42	1.76	2.75	7.23	1.2	3.16	3.12
ciliated.cell	0.88	0.1	0.24	0.84	0.39	0.22	4.96	0.83
dendritic.cell.type.1	1.06	2.68	1.86	1.49	1.1	0.69	2.05	1.45
dendritic.cell.type.2	1.71	3.13	4.55	5.09	1.64	4.15	1.5	2.95
fibroblast_a	1.07	4.53	4.58	0.61	4.46	4.59	5.24	3.36
fibroblast_b	2.06	11.41	17.16	17.7	16.12	19.73	10.74	12.61
fibroblast_c	21.16	1.29	1.69	0.37	0.43	2.82	0.84	5.97
lymph.vessel.cell	1.48	1.81	1.21	0.95	0.89	0.78	0.81	1.18
macrophage_a	15.32	0.16	0.24	0.14	0.2	1.17	0.84	3.95
macrophage_b	12.67	0.11	0.3	0.53	0.63	0.89	0.35	3.36
macrophage_c	0.86	6.17	3.45	1.53	7.26	5.11	9.36	4.39
macrophage_d	0.25	2.36	6.79	7.16	5.03	1.16	2.78	3.18
mast.cell	0.95	0.42	0.28	1.33	0.97	0.95	0.92	0.84
muscle.cell	0.31	1.14	0.64	2.04	2.67	0.45	2.92	1.27
natural.killer.cell	0.99	3.42	6.39	1.16	1.91	7.19	3.5	3.3
neutrophil	1.17	1.39	2.53	2.44	0.38	6.36	1.11	2.18
plasma.cell	1.51	11.47	8.01	1.36	3.1	4.33	2.21	4.38
plasmacytoid.dendritic.cell	1.61	2.38	1.94	2.08	1.59	2.08	1.3	1.85
regulatory.T.cell	6.61	0.24	0.4	0.75	2.51	0.41	1.96	2.36

Supplementary Fig.1a. CosMx FOV placements.

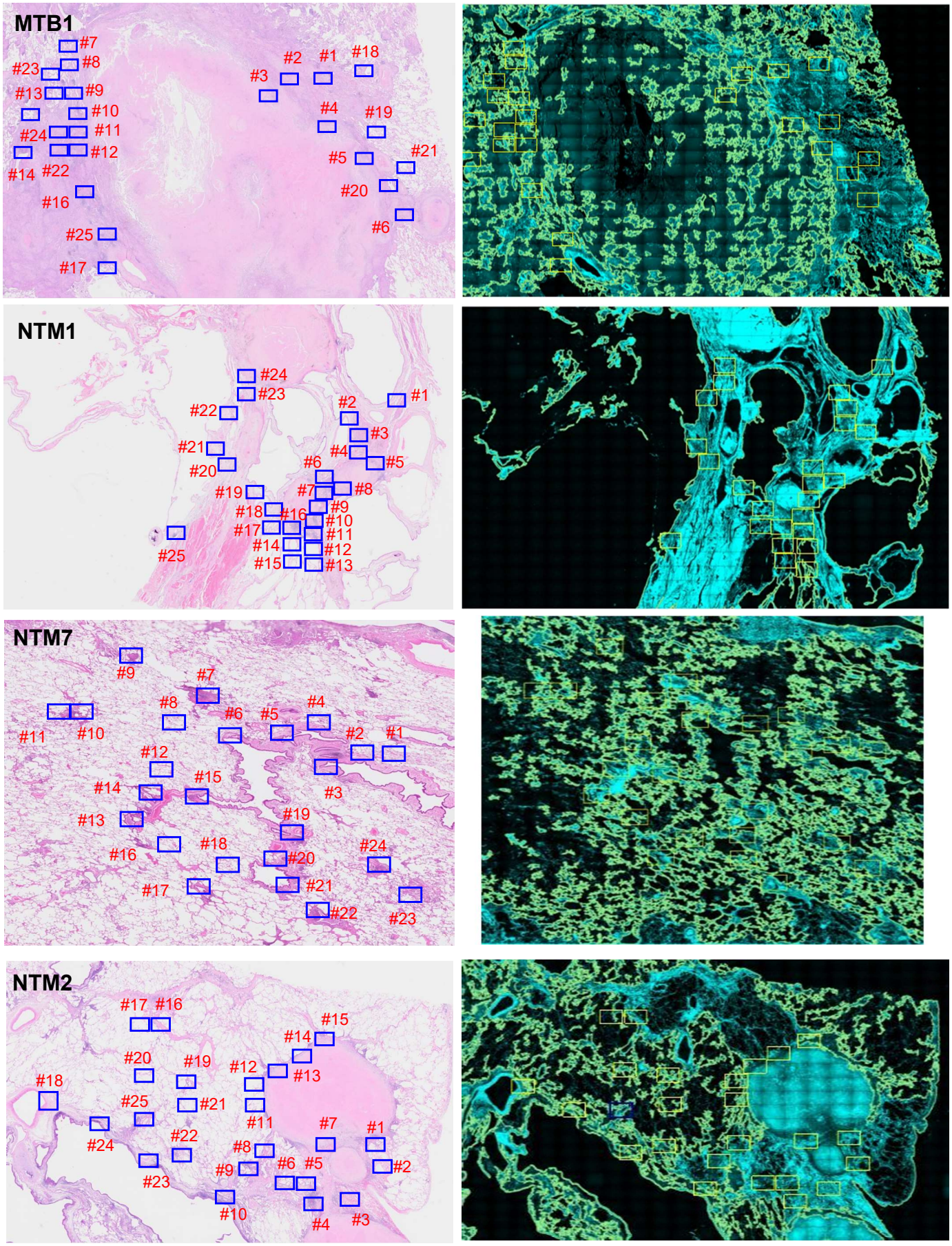

Supplementary Fig.1b. CosMx FOV placements.

MTB3

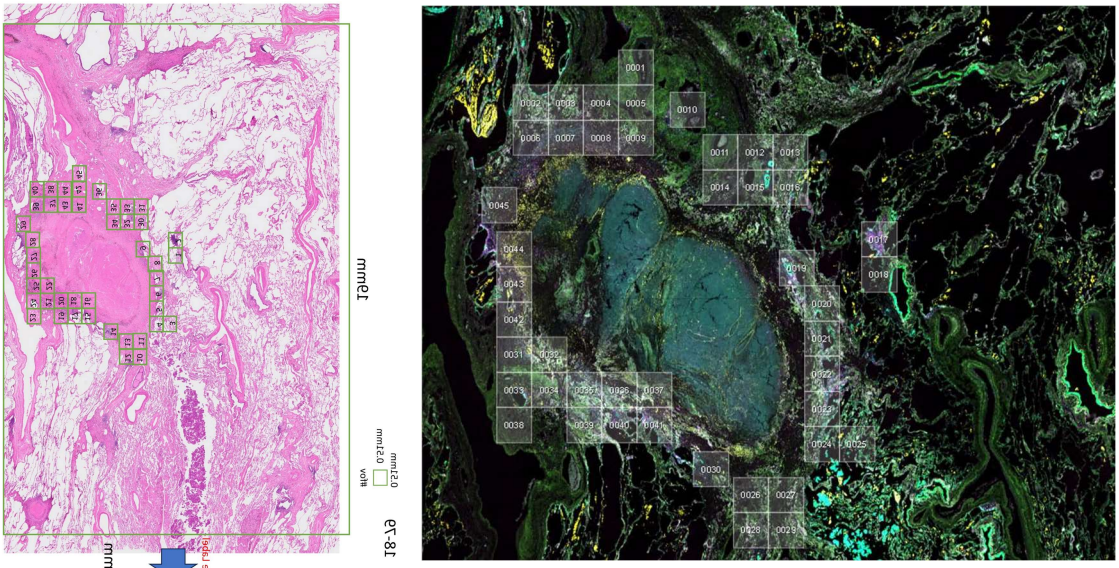

MTB2

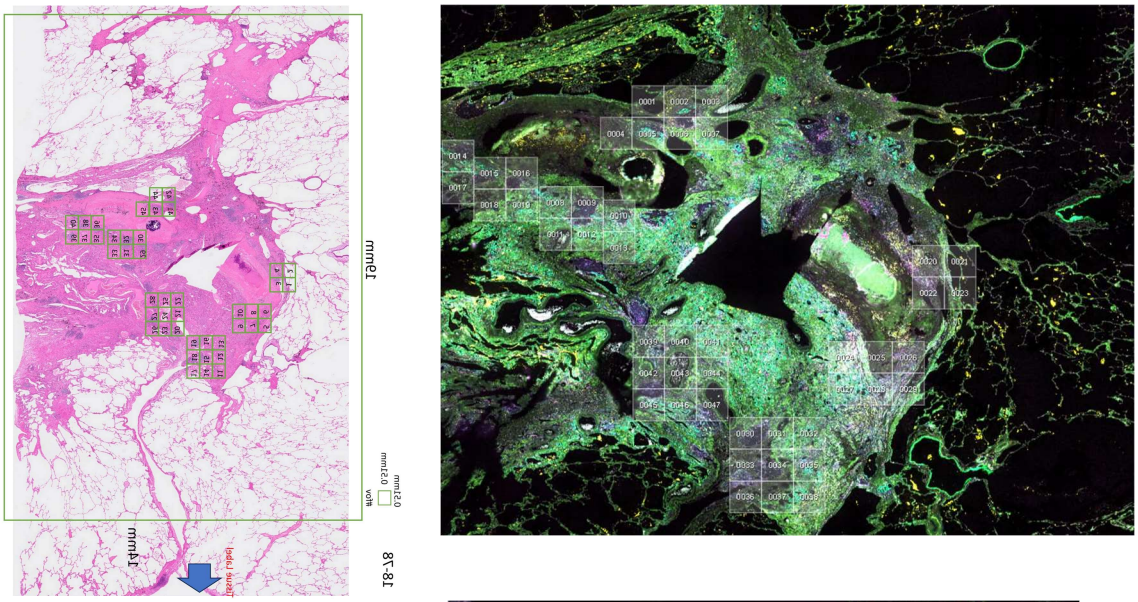

NTM3

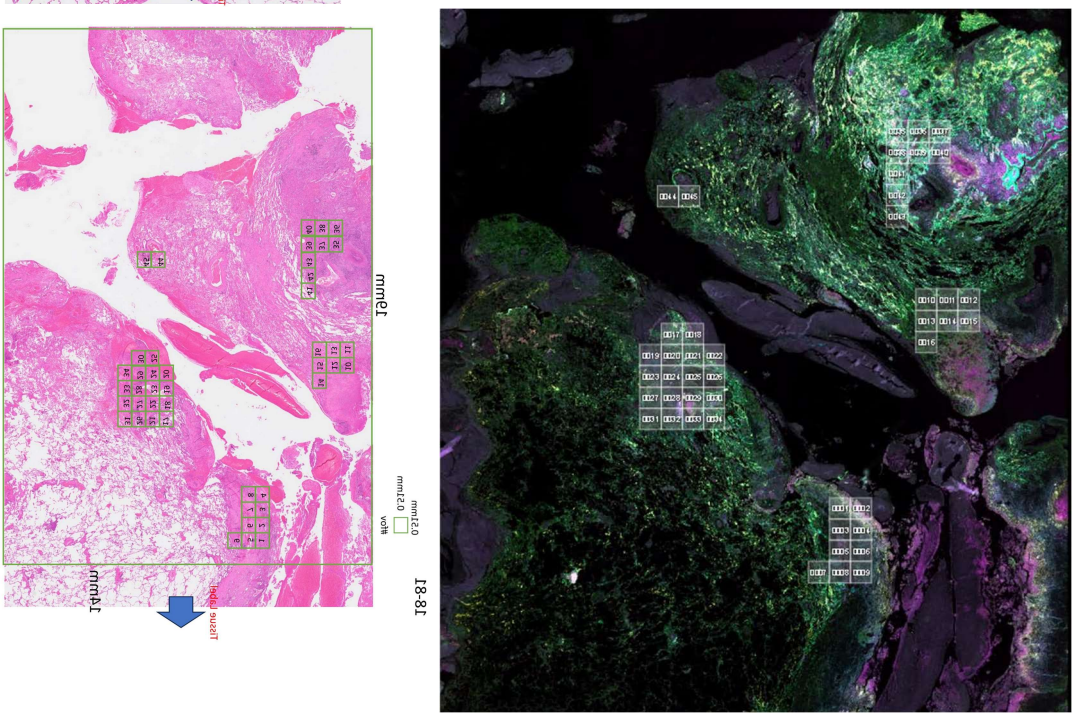

Supplementary Fig. 2: Immunohistochemistry for BCG. Blue and red boxes (right panels) show the enlarged images of left panels.

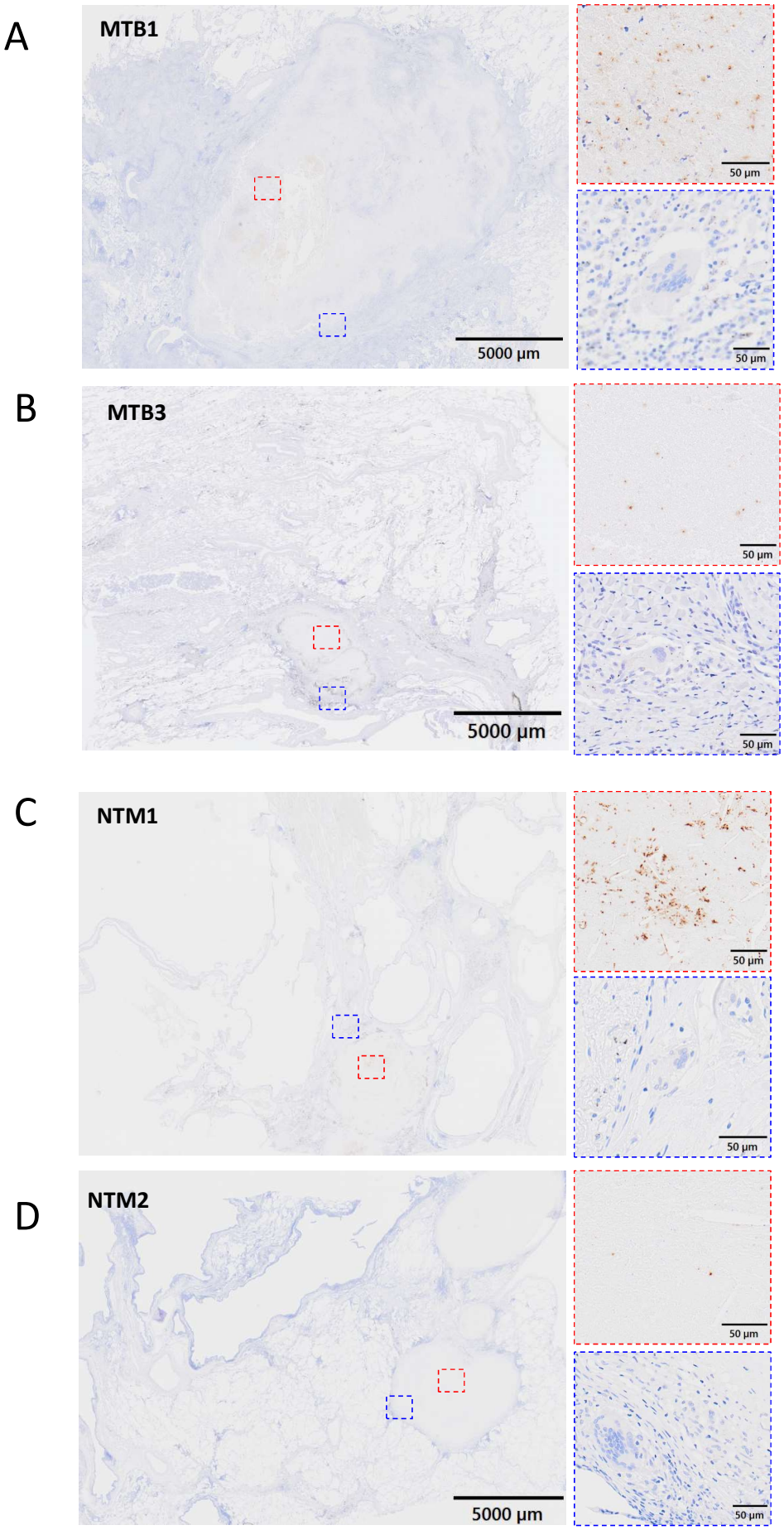

Supplementary Fig. 3: Each cell type in UMAP.

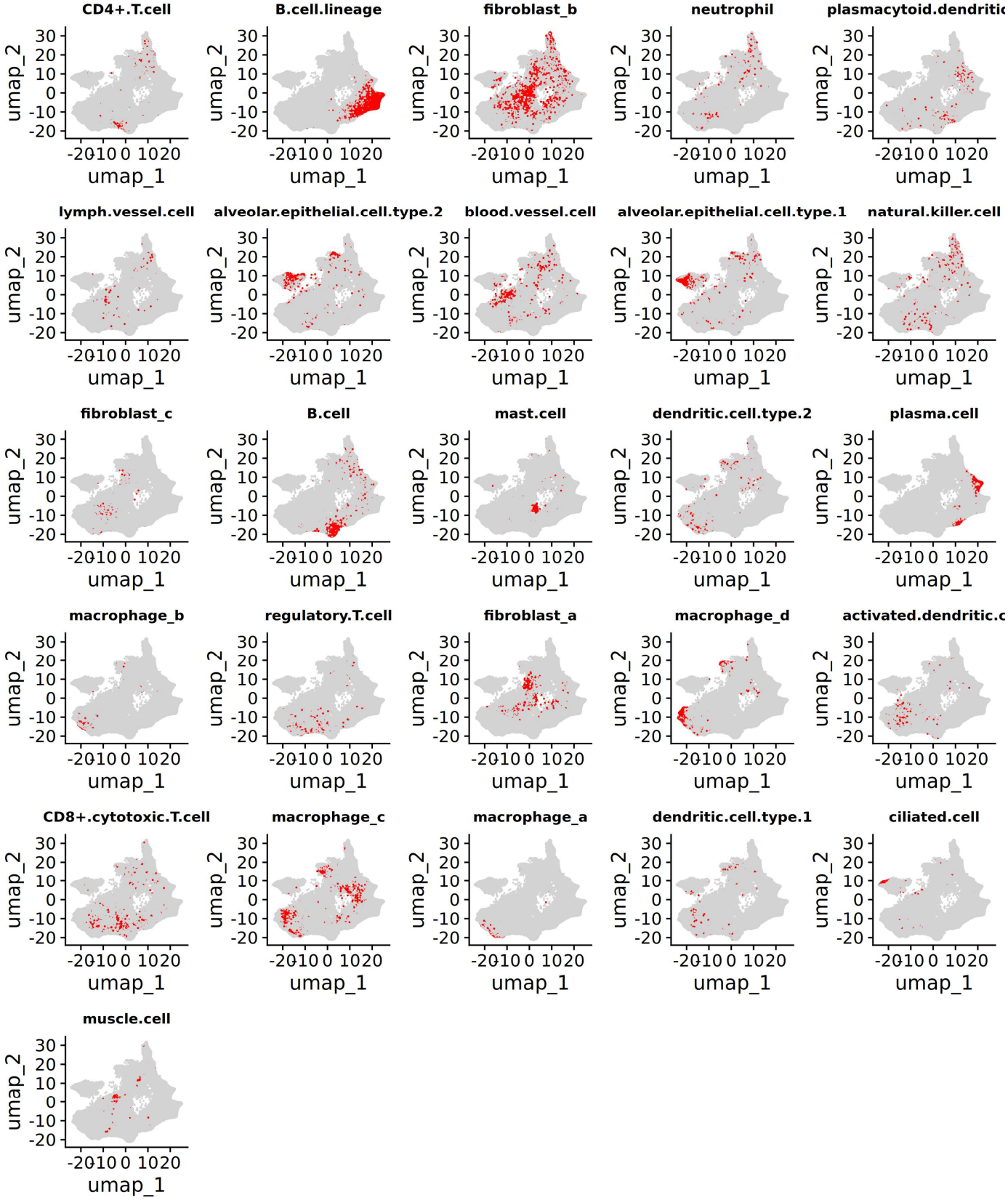

Supplementary Fig. 4: UMAP and population of each cell type. A. UMAP of each tissue. B. Populations of cell types in each tissue.

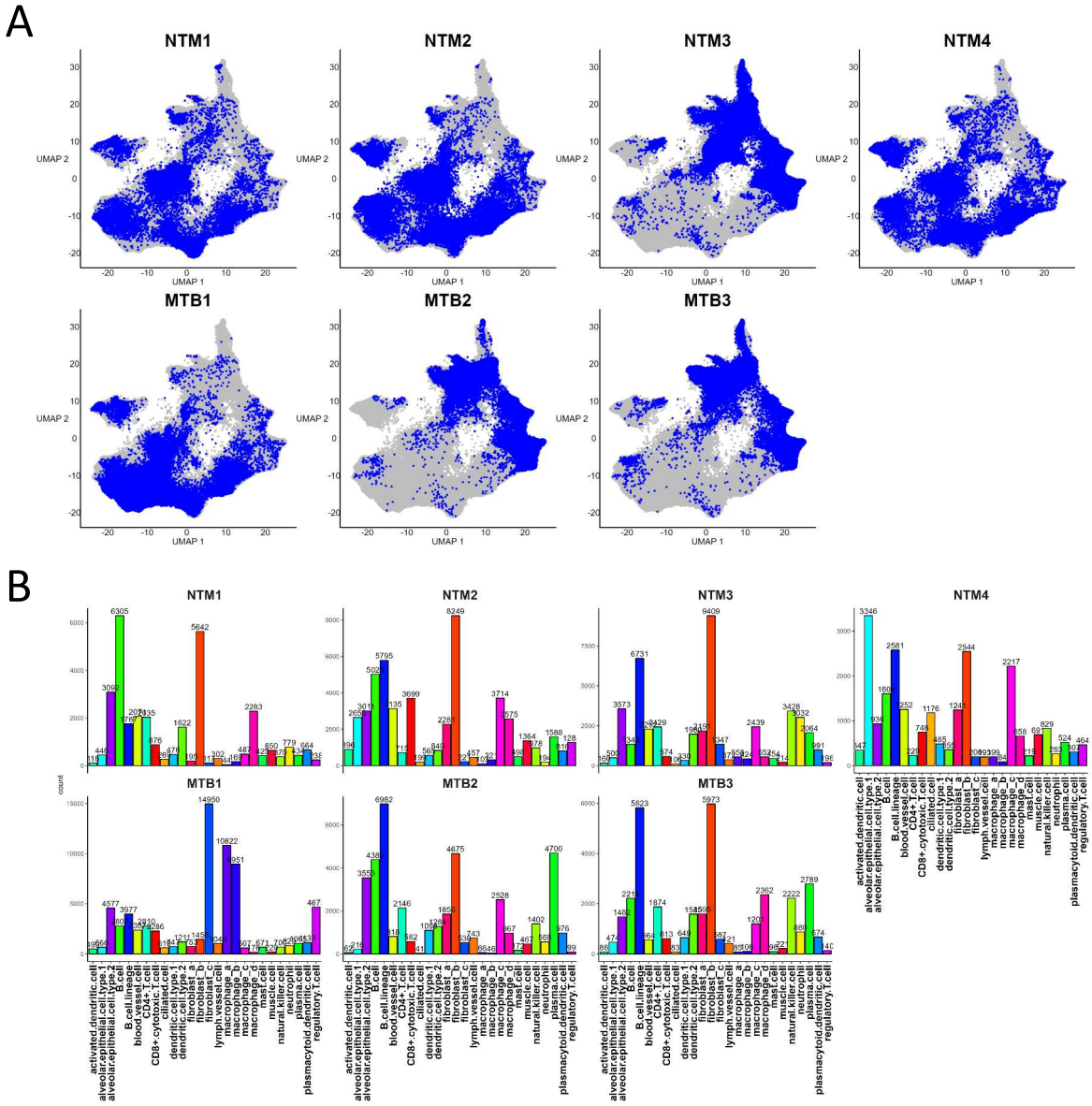

Supplementary Fig. 5: Distribution of cell type in FOVs of each slide

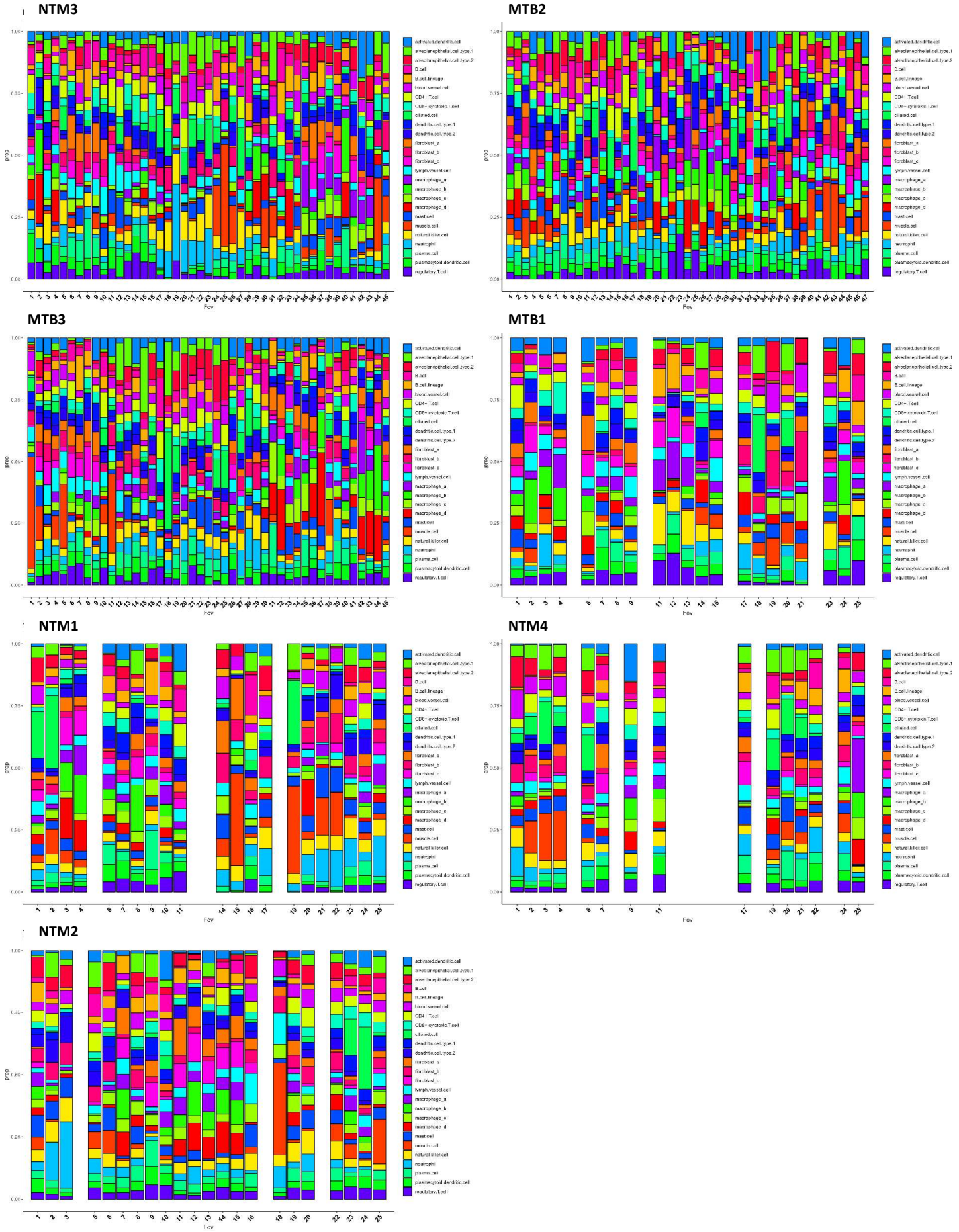

Supplementary Fig. 6a. CosMx spatial images of SPP1 and MARCO expression in macrophage_d in MAC+ tissue (NTM2 FOV9). A. Macrophage_d in the interstitial region expressed SPP1 and MARCO. B. Enlarged images of A. Colors indicating cell types are shown in the bottom panel.

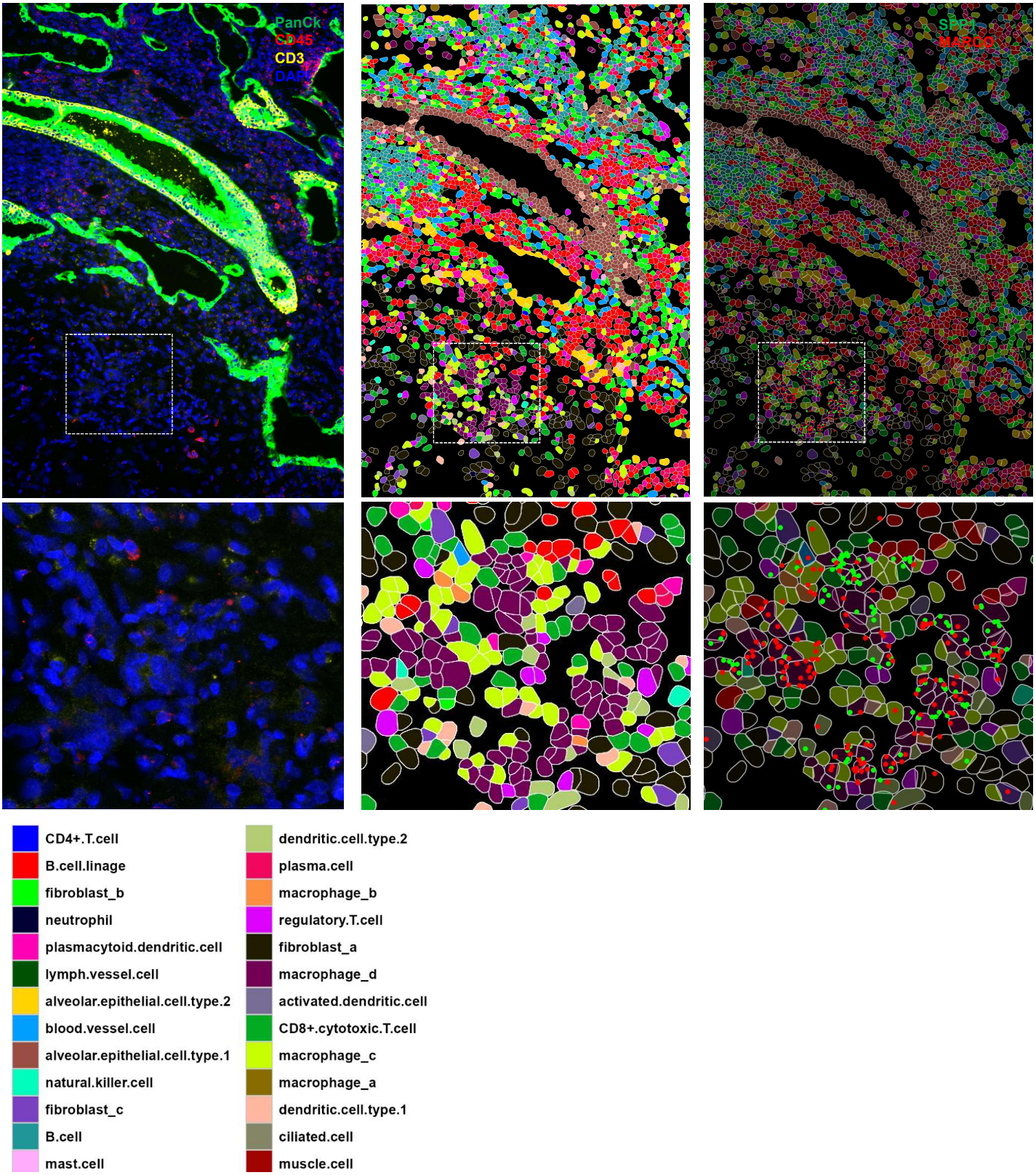

Supplementary Fig. 6b. CosMx spatial images of SPP1 and MARCO expression in macrophage_d in MAC+ tissue (NTM2 FOV8). SPP1-positive macrophages were found in alveolar space. A. Macrophage_d in the alveolar space expressed SPP1 and MARCO. B. Enlarged images of A. Colors indicating cell types are shown in the bottom panel.

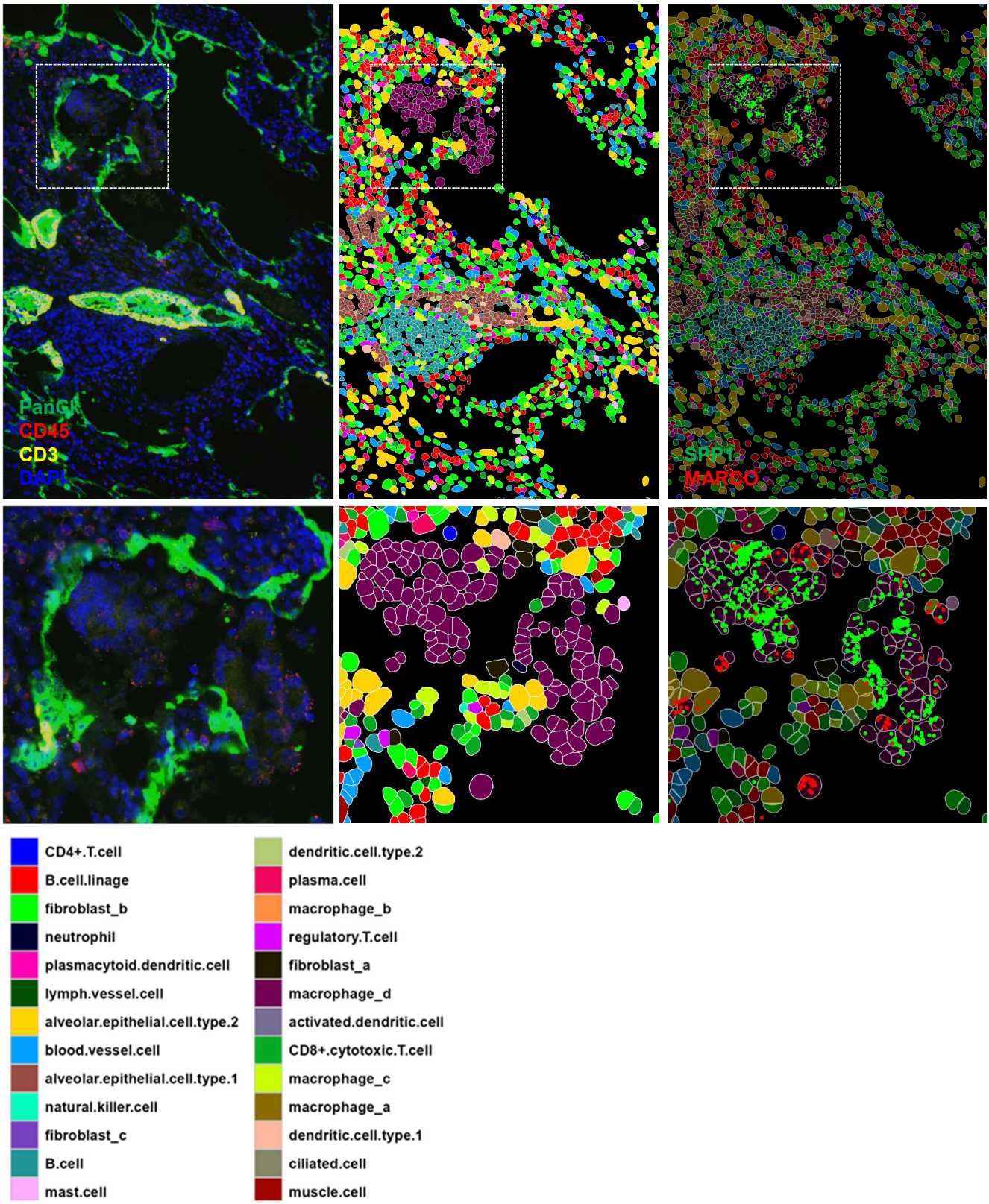

Supplementary Fig. 6c. CosMx spatial images of SPP1 and MARCO expression in macrophage_d in MTB+ tissue (MTB1, FOV24). A. Macrophage_d in the interstitial region expressed SPP1 and MARCO. B. Enlarged images of A. Colors indicating cell types are shown in the bottom panel.

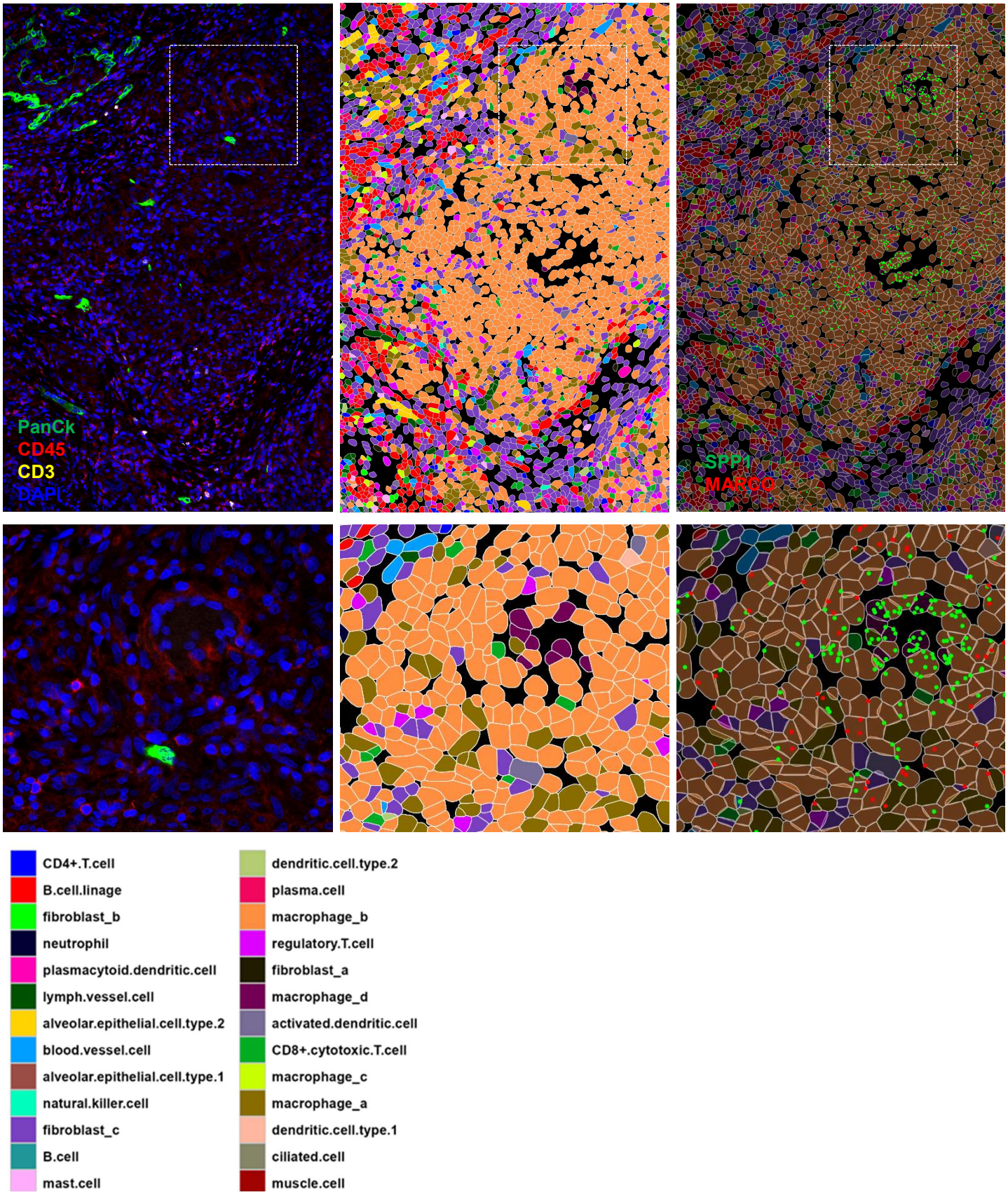

Supplementary Fig. 7. CosMx spatial images of SPP1 and CD44 expression in MTB and NTM tissues. Colors indicating cell types are shown in the bottom panel.

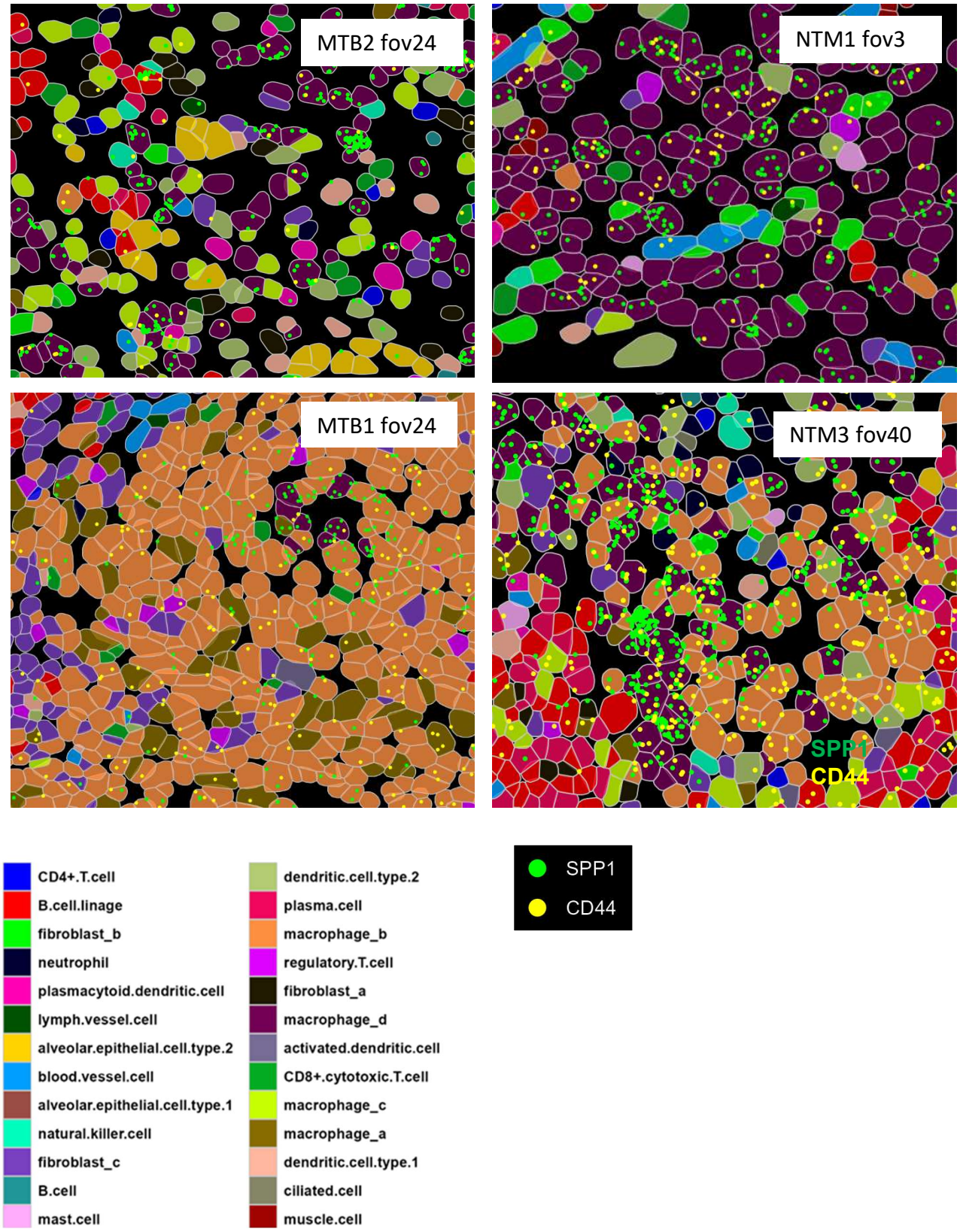

Supplementary Fig. 8: InSituCor analysis in MTB and NTM samples. A. Example of a cell's nearestneighbors, used to define its "environment expression" profile. B. Subset of the environment expression matrix. C. Raw correlation matrix of the environment expression matrix showing near-ubiquitous correlations (subset of 300 random genes).D. Correlation matrix of the environment expression matrix (B) conditional on the confounding matrix, over the same subset of genes as (C). E. Raw vs. conditional correlation of environment gene expression. Selected pairs of marker genes are highlighted. F. Network representation of correlation between all genes in all modules. Genes with correlation > 0.2 are connected. The module from Fig.7A is highlighted. G. Correlation structure of 51 ligands assigned to modules. Edges show conditional correlations > 0.1,and color shows module membership.

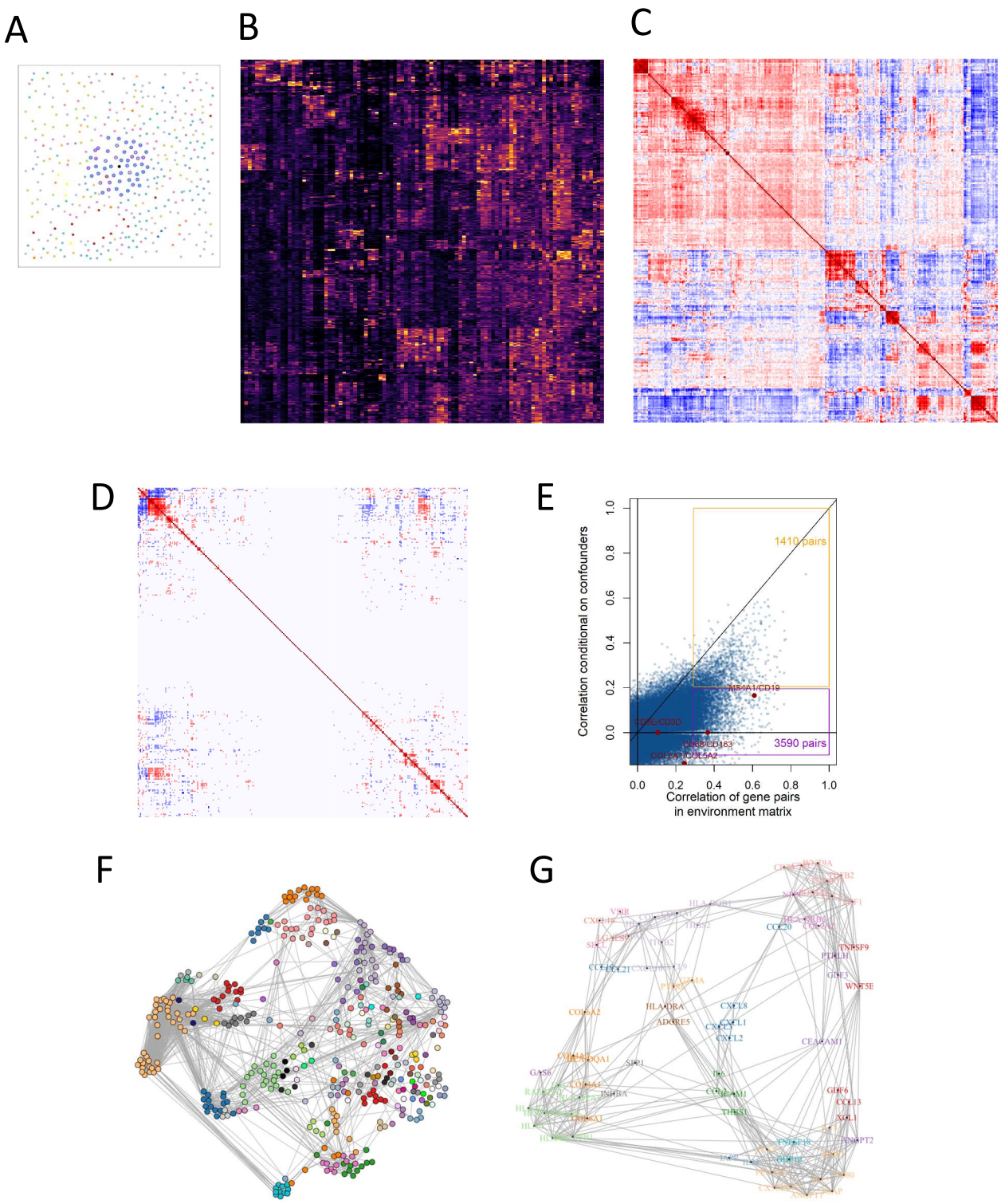

Supplementary Fig. 9: Outgoing and incoming communication patterns of secreting cells by cellchat analysis in MTB and NTM samples. A. River plot of cell (left panel) and cell-communication (right panel) pattern for outgoing signal pathways. B. Heatmaps of cell (upper panel) and cell-communication (lower panel) pattern for outgoing signal pathways. C. River plot of cell (left panel) and cell-communication (right panel) pattern for incoming signal pathways. D. Heatmaps of cell (upper panel) and cell-communication (lower panel) pattern for incoming signal pathways. E. Dot plots of incoming and outgoing interaction strength of each cell-cell communications in all ligand-receptor interactions.

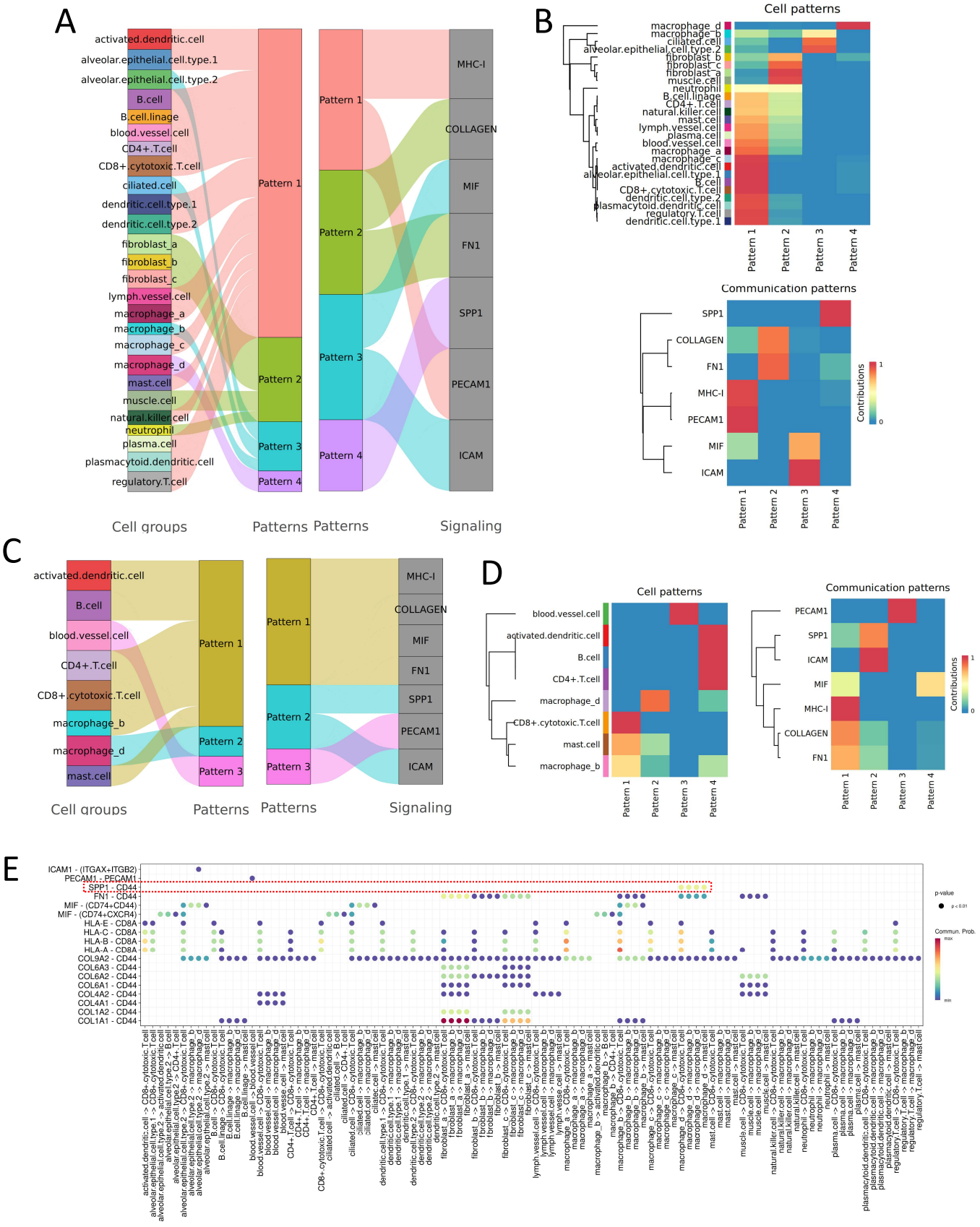
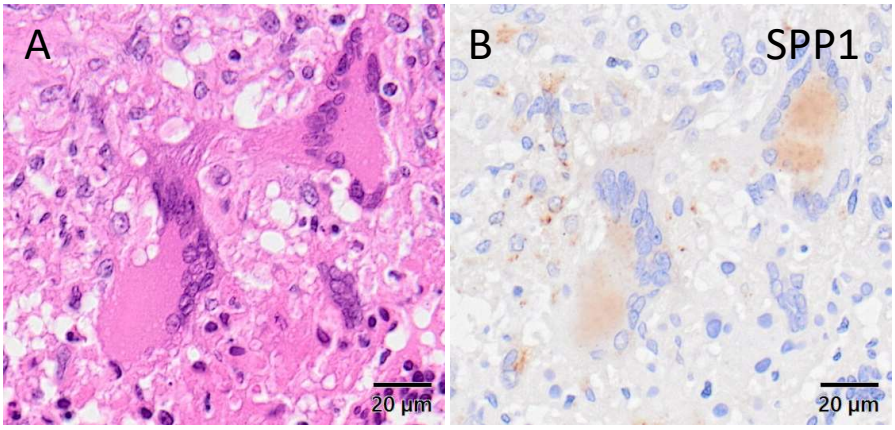
Supplementary Fig. 10: SPP1 expression in a tissue from a patient with Aspergillus pneumonia. A. HE. B. Immunohistochemistry for SPP1.